1T Phase Transition Metal Dichalcogenides for Hydrogen Evolution Reaction

Liang Chang, Zhuxing Sun & Yun Hang Hu

Electrochemical Energy Reviews

ISSN 2520-8489
Volume 4
Number 2

Electrochem. Energ. Rev. (2021)
4:194-218
DOI 10.1007/s41918-020-00087-y

Electrochemical Energy Reviews (2021) 4:194–218
https://doi.org/10.1007/s41918-020-00087-y

REVIEW ARTICLE

1T Phase Transition Metal Dichalcogenides for Hydrogen Evolution Reaction

Liang Chang[1] · **Zhuxing Sun**[1] · **Yun Hang Hu**[1]

Received: 18 August 2020 / Revised: 24 October 2020 / Accepted: 20 November 2020 / Published online: 22 January 2021

Abstract

Metallic (1T) phases of transition metal dichalcogenides (TMDs) are promising alternatives for Pt as efficient and practically applicable hydrogen evolution reaction (HER) catalysts. Group 6 1T TMDs are the most widely studied due to their impressively higher HER activity than that of their 2H counterparts. However, the mediocre electrochemical and thermal stability of these TMDs has limited their widespread application. Over the last decade, while immense attempts have been made to enhance the stability of group 6 1T TMDs, 1T TMDs based on other transition metals have gained increasing attention. To address the great potential of the 1T TMD family for industry-scale HER and inspire future breakthroughs in realizing their scalable utilization, a critical overview of 1T TMDs for application in HER is presented in this work. With an emphasis on the recent progress, the main contents include the elucidation of the "structure–performance" relationship in 1T TMD-based HER, the approaches for the synthesis and morphology control of 1T TMDs, and the types of 1T TMD-based materials that have been explored for efficient and long-term water splitting. Before the main discussions, the reaction mechanism of HER and the evaluation indexes for HER catalysts are introduced. Moreover, future perspectives on overcoming the primary challenges that hinder the practical application of 1T TMDs for HER are provided.

Keywords Transition metal dichalcogenides · 1T phase · Hydrogen evolution reaction · Electrocatalysis

1 Introduction

Hydrogen is the molecule with the highest energy density per unit mass. Even though the storage of hydrogen elements on earth is abundant, that of free hydrogen molecules is rather limited. Efficient and sustainable production of hydrogen is the key to widespread utilization of hydrogen [1–3]. Several technologies for hydrogen production have been explored, including steam or dry reforming of methane/methanol [4–8], photo- or electro-catalytic water splitting [9–13], the most recent thermo-photo-hybrid water splitting [8, 14–16], etc. Among them, electrocatalytic water splitting, which could make use of the electricity generated by intermittent renewable energies, shows great promise for large-scale and green hydrogen production [17]. Currently, Pt-group metals are recognized as the best electrocatalysts for hydrogen evolution reaction (HER). However, the high cost and limited storage of these materials have hindered their extensive application. For scalable hydrogen production from electrocatalytic water splitting, it is imperative to find low-cost and abundant alternatives to Pt.

Besides noble metals, the most investigated HER catalysts include transition metals, transition metal chalcogenides/phosphides/carbides/nitrides, and some metal-free catalysts [18]. Transition metals (i.e., Ni, W, Mo, Fe, and Cu) that possess Gibbs free energy of hydrogen adsorption far away from thermoneutral display sluggish hydrogen production. The metal-free catalysts, especially nanocarbon or carbon nitrides, require the additional electron modulation via heteroatom doping or substitution, and their HER activity, to some extent, is limited by the doping level and the distribution of heteroatoms. Transition metal chalcogenides (TMDs), phosphides (TMPs), carbides (TMCs), and nitrides (TMNs) are receiving the largest amount of attention due to their Pt-like HER behavior and relatively low cost.

Among the transition metal compounds, TMDs, the investigation on which could trace back to the 1970s [19], have gained increasing interest in the last two decades due to their great potentials for application in electrocatalysis

✉ Yun Hang Hu
yunhangh@mtu.edu

[1] Department of Materials Science and Engineering, Michigan Technological University, Houghton, MI 49931-1295, USA

[17], photocatalysis [20], supercapacitors [21], solar cells [22], memristors [23, 24] and so forth. There are multiple polymorphs for TMD materials. Figure 1a demonstrates the most well-known three polymorphs of TMDs, i.e., 2H, 1T, and 1T′ [25]. All the three phases possess a lamellar structure with one layer of transition metal atoms (M) sandwiched between two layers of chalcogenide (X) atoms. The hexagonal 2H phase with the chalcogenide elements in trigonal prismatic coordination (D_{3h}) around the metal atom is the most commonly observed for all group 6 TMDs (except WTe_2) under ambient conditions. The metallic 1T phase is a one-layer stack in the tetragonal symmetry with octahedral coordination (D_{3d}). The distorted 1T phase with metal atoms bonded in the form of zigzag chains is called 1T′ phase. Transition among the three phases could take place with geometric rotations [25, 26]. The transversal displacement of one X layer induces the phase transition from 2H to 1T, while further distortion of the M chains in 1T phase yields 1T′ phase. Along with the atom rearrangement, the electronic and catalytic properties of TMDs are altered as well [27–29].

The intriguing materials, represented by group 6 TMDs, have been extensively explored for HER in the past fifteen years. The HER active sites of 2H group 6 TMDs locate at sulfur edges of MX_2 with the zigzag or armchair distribution. At H coverage of 50%, the hydrogen binding energy at zigzag edges is about 0.08 eV, very close to the optimum value of 0 eV [30, 31]. However, the inert basal plane and the semiconducting feature of 2H TMDs limit their HER performance. Even though the edge/basal ratio can be increased by constructing amorphous, few-layer, or nano-sized structures with rich exposed edges [32–36], the reduction in conductivity would bring a marginal improvement [37]. For 1T/1T′ TMDs, both their edges and basal planes are electrocatalytically active. Meanwhile, the (semi)metallic characteristic and large surface area of the 2D 1T/1T′ TMDs ensure the fast transfer of electrons and the large abundance of active sites, respectively. Thereby, 1T/1T′ TMDs have been regarded as promising alternatives to Pt for industry-level HER.

Due to the intriguing properties of 1T/1T′ TMDs, the synthesis approaches and applications of 1T TMDs, especially 1T MoS_2, have been comprehensively discussed in several excellent review articles [38, 39]. However, a specific overview of 1T/1T′ TMD materials for HER is still lacking. Herein, considering the great importance of 1T/1T′ TMD materials for HER, the "structure–performance" relationship of various 1T TMDs for HER is delineated, following a brief introduction of HER mechanism and the evaluation of HER catalysts. Furthermore, based on the "structure–performance" relationship, the recent progress in the controlled synthesis of 1T/1T′ TMDs and the construction of 1T/1T′ TMDs-based materials for efficient and stable HER are thoroughly discussed. Also, key challenges and perspectives in

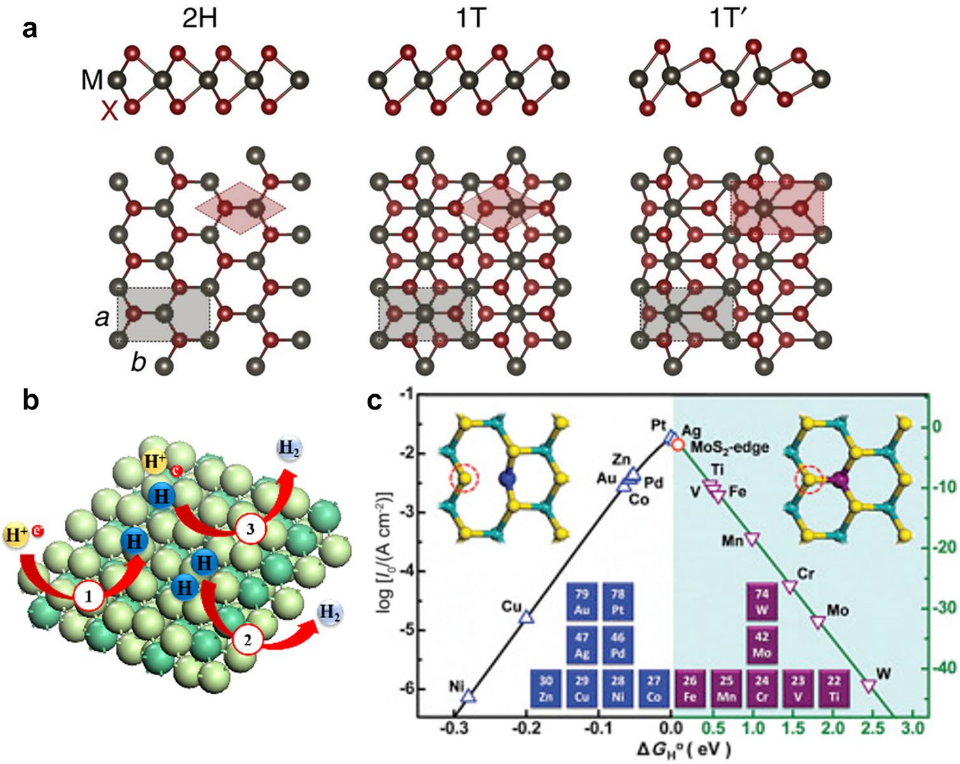

Fig. 1 **a** The top schematics show cross-sectional views, and the bottom schematics show basal plane views. Reproduced with permission from Ref. [25]. Copyright 2016, Springer Nature. (**b**) Illustration of HER mechanism (① Volmer reaction, ② Tafel reaction, and ③ Heyrovsky reaction); **c** volcano plot of the exchange current density as a function of the DFT-calculated Gibbs free energy of adsorbed atomic hydrogen for MoS_2 and the pure metals. Reproduced with permission from Ref. [48]. Copyright 2017, Elsevier

further developing supreme 1T TMDs into commercially usable electrocatalysts are typically addressed at the end. The content is intended to inspire more breakthroughs in engineering advanced 1T TMDs materials for practically applicable HER.

2 Fundamentals of HER

2.1 General Mechanism

HER takes place on the electrode surface via two separate steps, that is, the adsorption of hydrogen ions (the Volmer step) and the desorption of hydrogen molecules (the Heyrovsky or the Tafel step) [40, 41]. Depending on the protons coming from hydronium cations (H_3O^+) in an acidic electrolyte or water molecules in an alkaline solution [42], the two-electron transfer reaction of HER follows the different pathways. For the acidic condition (Fig. 1b), in the Volmer step, an adsorbed hydrogen atom (H*) is formed when a proton (H^+) adsorbed on an empty active site (*) is coupled with an electron (e^-). The process can be expressed as $H^+(aq) + * + e^- \rightarrow H^*(ads)$. The subsequent production of H_2 could take place via either the chemical combination of two surface adsorbed hydrogen atoms or the direct bonding of a hydrated proton, a transferred electron, and an adsorbed hydrogen atom. The former one is known as the Tafel or recombination reaction [$H^*(ads) + H^*(ads) \rightarrow H_2(g)$], and the latter one is called the Heyrovsky or ion + atom reaction [$H^+(aq) + e^- + H^*(ads) \rightarrow H_2(g)$] [20, 43]. For an alkaline medium, the Volmer and the Heyrovsky reactions are expressed as $H_2O + * + e^- \rightarrow H^*(ads) + OH^-$ and $H_2O + e^- + H^*(ads) \rightarrow H_2 + OH^-$, respectively. In some cases, the Volmer step is divided into two steps, i.e., the dissociation of H_2O and the formation of H* intermediates [44].

Generally, the alkaline electrolyte, which allows the oxidation and reduction of water under the same condition, can eliminate pH-induced energy and ion exchange consumption. However, the unfeasible release of the proton from water dissociation, which is related to the high-energy barrier for water dissociation (ΔG_{H_2O}) on the catalyst surface, makes the HER kinetics in alkaline solutions much slower than that in acidic mediums [45]. As a result, the HER rates of most transition metals, including Pt, Ir, and Pd, in the base are two orders of magnitude slower than those in the acid [46]. Nevertheless, in a strong alkaline solution [> 1 M (1 M=1 mol L^{-1})], a local acid-like environment could be generated on nanostructured catalytic surfaces, leading to efficient HER [3].

2.2 Sabatier Principle

The Sabatier principle suggests that an efficient reaction relies on an appropriate (not too strong or too weak) interaction between the catalyst surface and the reactive intermediates. As for HER, the Gibbs free energy of hydrogen adsorption (ΔG_{H*}) can be the descriptor for the adsorption of H and the desorption of H_2 on a catalyst surface. The ideal HER catalyst is supposed to show a $\Delta G_{H*} \approx 0$ [47]. The negative shift of ΔG_{H*} indicates a strong hydrogen bonding on a catalyst surface and thus the rate-determining step of Heyrovsky or Tafel, whereas the positive shift of ΔG_{H*} corresponds with a weak hydrogen–catalyst bonding, making the Volmer step slower. A "volcano plot" (Fig. 1c) can be obtained when depicting the exchange current densities for various catalysts as a function of ΔG_{H*} [48]. Typically, a catalyst that locates closer to the peak around $\Delta G_{H*} = 0$ could achieve a better HER activity.

2.3 Evaluation of the HER Catalysts

An HER catalyst is commonly evaluated by the polarization (i–E) curve acquired from linear sweep voltammetry (LSV). On the IR-corrected polarization curve, the current density (j) at a certain overpotential (η) can reflect the apparent activity of the HER electrode. The two key factors are the onset potential at a current density of 0.5 or 1 mA cm^{-2} and the overpotential at 10 mA cm^{-2} (η_{10}), which can be read directly from the i–E curve [49]. Other indexes, like exchange current density (j_0) and the Tafel slope (b), can be calculated by the Butler–Volmer equation [50]:

$$j = j_0 \left[e^{(1-\sigma)\eta f} - e^{-\sigma \eta f} \right] \tag{1}$$

where j_0 is the exchange current density, σ the transfer coefficient, and $f = F/RT$ (R is the ideal gas constant, T the temperature, and F the Faraday constant.). At $\eta > 0.05$ V, the Butler–Volmer equation can be simplified to the Tafel equation:

$$\eta = b \log \left(j/j_0 \right) \tag{2}$$

Herein, j_0 is extracted from the i-axis intercept of the linear-fitted i–E curve and reflects the rate of electron transfer under reversible conditions (that is, at zero overpotential). And the Tafel slope (b), which suggests the potential difference that is needed to change j by ten times, reveals the reaction mechanism of a catalyst. Theoretically, Tafel slope can be expressed as

$$b = \frac{2.3RT}{(n' + \alpha)F} \tag{3}$$

where n' is the number of electrons transfer before the rate-determining step and α the exchange transfer coefficient (0–1) [51]. Accordingly, the value of the Tafel slope can be used to judge the rate-determining step of an HER process. When the rate-determining step is the Tafel reaction, b should be around 29 mV dec^{-1} ($\frac{2.3RT}{2F}$) at 25 °C. If the Heyrovsky reaction limits the reaction rate, b around 38 mV dec^{-1} ($\frac{4.6RT}{3F}$) could be observed. While the rate-limiting step is the Volmer reaction, the Tafel slope will be rather large with $b = \frac{4.6RT}{F}$ (116 mV dec^{-1}).

Apart from the apparent activity of an electrode, the intrinsic activity of each catalytic site is another important metric for an electrocatalyst, which can be assessed by the turnover frequency (TOF, s^{-1}).

$$\mathrm{TOF} = \frac{jA}{nFN} \tag{4}$$

In this equation, j is the current density at a given potential, A Avogadro's number, n the number of electrons transferred (2 for HER), and N the density of active sites [52]. Considering the difficulties in determining the reaction rate and counting the active sites, a reliable comparison for TOF conducts at a specific potential or zero overpotential [53].

Besides, electrochemical impedance spectroscopy (EIS) operated under HER voltage helps probe the HER kinetics and analyze the electrode/electrolyte interface interaction. Generally, the solution resistance (R_s), charge transfer resistance (R_{ct}), and double-layer capacitance (C_{dl}) can be derived from Nyquist plots and used for obtaining an equivalent circuit [54]. Furthermore, the stability of an HER catalyst can be measured by repetitive LSV scans or a chronoamperometry test over 10 h. And its faradaic efficiency can be assessed by experimentally produced H_2, that measured by gas chromatography, over theoretically calculated H_2 [55].

According to previous studies on 1T TMD electrocatalysts, HER generally followed the Volmer–Heyrovsky mechanism [56]. Optimal 1T TMDs electrocatalysts should have small onset potential, η_{10}, and Tafel slope, and large TOF and Faraday efficiency. More detailed analysis will be discussed case-by-case in the following sections.

3 Structure–Performance Relationship of 1T TMDs for HER

For the various 1T TMDs with different transition metals (Ti, V, Nb, Ta, Mo, W, Pd, and Pt) and chalcogens (S and Se), their HER activities are distinct from each other. Theoretical studies by Tsai et al. [56] revealed that the metallicity of a TMD basal plane is more important than structure and composition in determining the HER activity. But the activity and stability relationship at edges are similar for the diverse TMDs regardless of the phase and chalcogen. This section discusses the structure–performance relationship of various TMDs for HER.

3.1 Group 6 1T TMDs

TMDs based on group 6 elements (Mo, W) have been widely explored for HER. The superior HER performance of 1T phase to that of its 2H counterpart was first demonstrated by Lukowski et al. [57] with *n*-butyllithium chemically exfoliated MoS_2 nanoflowers. The obtained 1T MoS_2 showed a η_{10} of 187 mV and a Tafel slope of 43 mV dec^{-1}. Almost at the same time, Chhowalla and coworkers chemically exfoliated bulk WS_2 nanosheets into strained metallic 1T (1T′) phase WS_2, obtaining an even lower η_{10} of 100 mV, a close Tafel slope of 60 mV dec^{-1}, and a TOF of 175 s^{-1} at −288 mV in 0.5 M H_2SO_4 [58]. However, with 1T′ WS_2 further treated at increasing temperatures, the current density of the material for HER decreased proportionally (Fig. 2a), indicating the vulnerability of the active phase to thermal treatment [58]. As observed by high-angle annular dark-field (HAADF) imaging in the scanning transmission electron microscope (STEM), during the thermal annealing process, the atoms relaxed from distorted 1T (1T′) zigzag chain superlattice and rearranged to 2H structure (Fig. 2b, c) [58].

The phase-dependent HER activity of TMDs has been well recognized over the past years [38, 59, 60]. The 2H phase of group 6 MX_2 (M = Mo/W, X = S/Se) is only catalytically active at the edge sites, while both the basal planes and edges of 1T-MoS_2 show electrochemical activity [61, 62]. As a typical verification, Voiry et al. [63] selectively oxidized the edges of 2H- and 1T-MoS_2, respectively, by dipping them in an oxygen-saturated aqueous solution for a few days (Fig. 2d). 1T-MoS_2 and the edge oxidized 1T-MoS_2 showed a similar HER performance with $\eta_{10} = 100$ mV and the Tafel slope = 40 mV dec^{-1}, whereas the edge oxidized 2H MoS_2 exhibited significantly degraded performance compared with pristine 2H MoS_2 (Fig. 2e). Furthermore, Lukowski et al. [64] found that the increase of catalytic activity was an order of magnitude larger than that of electrochemically active surface areas when the as-grown 2H WS_2 bulk was chemically exfoliated into 1T-WS_2 nanosheets. This indicated that the improved activity was not only contributed by proliferated active sites. The high conductivity of the metallic 1T polymorph could also play an essential role in the outstanding performance [38]. Besides, H coverage is influential to HER activity. A theoretical study by Tang et al. [65] suggested that the catalytic activity of 1T-MoS_2 mainly arose from the affinity binding H at the surface S sites and reached the optimum with H coverage of 12.5%–25.0% (Fig. 2f).

Among the four representative 1T TMD materials—MoS_2, $MoSe_2$, WS_2, and WSe_2, WS_2 and $MoSe_2$ showed a more efficient 2H → 1T transition after chemical exfoliation

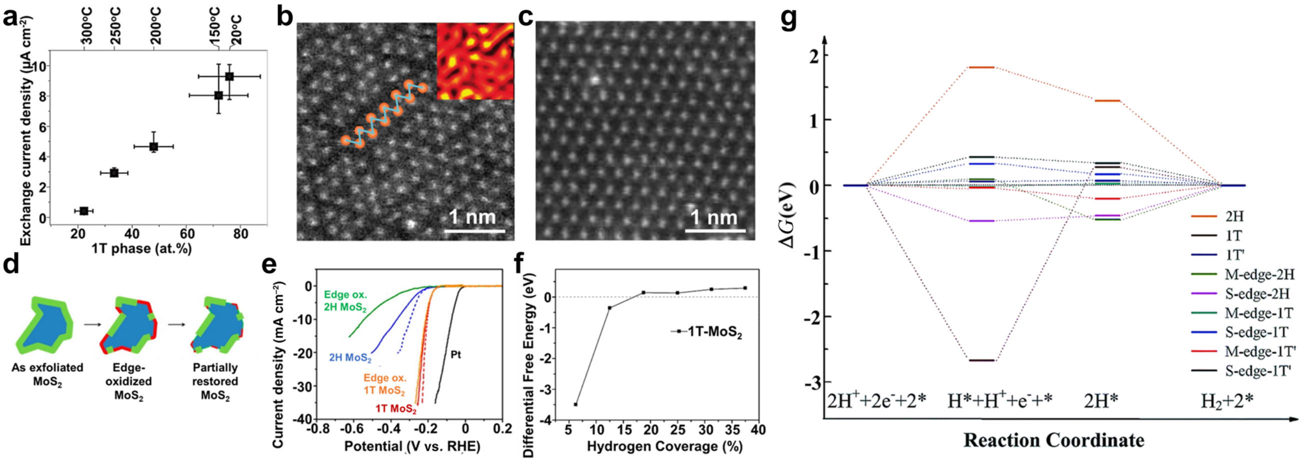

Fig. 2 **a** Catalytic activity as a function of the 1T phase concentration obtained by annealing in an inert atmosphere; high-resolution STEM images of an as-exfoliated WS_2 monolayer showing regions exhibiting the **b** 1T superlattice and **c** 2H structures. Reproduced with permission from Ref. [58]. Copyright 2013, Springer Nature. **d** Schematic of the oxidation process and partial restoration of the nanosheet edges after several voltammetry cycles; **e** polarization curves of 1T and 2H MoS_2 nanosheet electrodes before and after edge oxidation. IR-corrected polarization curves are shown by dashed lines. Reproduced with permission from Ref. [63]. Copyright 2013, American Chemical Society. (**f**) Calculated differential free energy of hydrogen adsorption (ΔG_H) as a function of hydrogen coverage on 1T-MoS_2 surface. Reproduced with permission from Ref. [65]. Copyright 2016, American Chemical Society. (**g**) Calculated Gibbs free energy profile of HER at the basal planes and edges of 1H, 1T, and 1T′ MoS_2. Reproduced with permission from Ref. [62]. Copyright 2014, The Royal Society of Chemistry

with *n*-butyllithium and thus a superior HER performance [66]. Meanwhile, Lukowski et al. [64] suggested the 1T phase-dominated nano-WS_2 showed the best HER performance in the nano-MX_2 family. In fact, in most cases, the 1T monolayers of Mo, W-based TMDs are unstable and easily transform to their metastable 1T′ phases, which, thus, are more frequently observed [62]. Via a high-resolution TEM, Chou et al. revealed a preferential transformation from 2H- to 1T′-MoS_2 occurred during lithium intercalation [67]. In addition, 1T′ phase possessed active basal planes and edge sites for HER, overweighing its 1H and 1T counterparts (Fig. 2g) [62]. Besides, it was found that while 1T′-WS_2 is metallic, 1T′-MoS_2 is semiconducting/semi-metallic with a very small bandgap of 0.1–0.2 eV [62]. But the relation between this difference and the HER performance has not yet been elucidated. Nevertheless, the energy barrier for 1T′ phase to transform to the corresponding 1H phase is substantially low (e.g., 0.7 eV for 1T′- to 1H-MoS_2). Upon thermal treatment or long-term electrochemical running, the phase change could take place and reduce the catalytic performance.

For the 1T/1T′ TMDs based on other group 6 metals, 1T′-$MoTe_2$ has demonstrated appreciable activities in acidic, neutral, and alkaline electrolytes with careful regulation of the phase, morphology, and the defect [68–76]. High-quality WTe_2 nanoribbon crystals with 1T′ Weyl semimetal phase have also been reported to show a Tafel slope of 57 mV dec^{-1} and an ultrahigh stability at 10 mA cm^{-2} in 5000 cycles and 20 h [77]. The HER performance of Cr-based TMDs has not been reported yet, albeit the synthesis and phase transition of 1T(1T′)-CrS_2, $CrSe_2$, and Cr_2Te_2 have been unveiled by the experimental and theoretical studies [78–80]. Nevertheless, admirable HER activity could be expected on 1T Cr-based TMDs because ultrahigh HER activity of the 2H-CrS_2 monolayer with S vacancies has been predicted by Sun et al. [81] according to first-principle calculation.

3.2 Other 1T TMDs

In addition to Mo/W-based TMDs, studies on other 1T TMDs, including group 4 TMDs like TiS_2 [82], group 5 TMDs like VS_2 [83–85] and TaS_2 [86, 87], group 7 TMDs like ReS_2 [88, 89], etc., have received increasing attention in the recent years for their physical and chemical properties distinctive to those of the group 6 TMDs.

Group 5 MX_2 (M = Nb, Ta, and V; X = S, Se, and Te) members are intrinsically metallic in either 1H or 1T phases and electrochemically active on their basal planes [90]. Among them, the VS_2 monolayer is currently known as the best HER catalyst with its performance comparable to that of Pt [91, 92]. The formation energy of 1H-VS_2 and 1T-VS_2 is very close with a difference of merely 0.04 eV/V atom. 1T-VS_2 is even stabler than H-VS_2 in bulk phases [93]. According to the theoretical calculation results by Fan et al. [94], at a high H coverage, 1H-VS_2

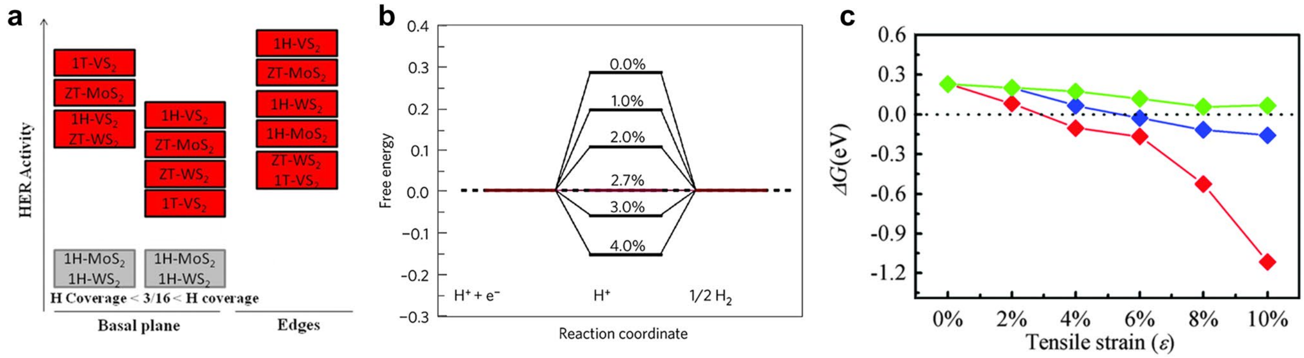

Fig. 3 **a** HER activity of MX_2 in basal planes and edges. Reproduced with permission from Ref. [94]. Copyright 2016, American Chemical Society. **b** Free-energy diagram for hydrogen evolution at equilibrium ($U=0$) with tensile strain in atomically thin 1T WS_2. The free energy of $H^+ + e^-$ was by definition equal to that of ½ H_2 at standard conditions (1 bar of H_2 and pH = 0 at 300 K). Reproduced with permission from Ref. [58]. Copyright 2013, Springer Nature. **c** Tensile strain dependent Gibbs free energies of H adsorption for monolayer 1T-MoS_2 (the coverage of H is 1/8). Red, blue and green diamonds refer to data of biaxial stretching, uniaxial stretching parallel to the zigzag lines and uniaxial stretching perpendicular to the zigzag lines, respectively. Reproduced with permission from Ref. [101]. Copyright 2016, The Royal Society of Chemistry

showed better HER performance than both 1H-MoS_2, 1T′-MoS_2, 1H-WS_2, 1T′-WS_2, and 1T-VS_2 (Fig. 3a). While with a low H coverage (< 3/16), the HER performance of 1T-VS_2 turned out to be the best. Overall, the HER activities of MoS_2, WS_2, and VS_2 are in the order of $VS_2 > MoS_2 > WS_2$ under standard conditions [94]. Experimentally, highly conductive 1T-VS_2 nanoflowers were reported to exhibit an ultra-low onset potential of 32 mV, a small overpotential of 58 mV at 10 mA cm^{-2}, a Tafel slope of 34 mV dec^{-1}, and faradaic efficiency of 100%, as well as high stability [84]. TaS_2, another group 5 TMD, has also received increasing attention. But, very different from the Mo/W-based TMDs, the 2H-phase TaS_2 shows a higher HER activity than its 1T counterpart, which was proved both theoretically [56] and experimentally [95].

As important members of group 7 material-based TMDs, rhenium dichalcogenides have a pristine distorted 1T (1T′) phase [96]. Since the basal planes of 1T′-$ReSe_2$/ReS_2 are inert, initial studies on ReS_2 and $ReSe_2$ for HER demonstrated substantially poor performance of these materials compared to that of Mo- and W-based TMDs. The vertically aligned ReS_2 nanosheets on Au required ~ 200 mV overpotential to achieve − 10 mA cm^{-2} current density and showed a Tafel slope of 84 mV dec^{-1} [97]. Hydrothermally obtained $ReSe_2$ nanosheets presented an η_{10} of ~ 320 mV and a Tafel slope of 67.5 mV dec^{-1} [98]. In contrast, the edge sites of 1T′-$ReSe_2$ are highly active for HER with ΔG_{H*} values were close to 0 (0.01–0.07 eV) [99]. To obtained abundant edge exposure, Zhuang et al. synthesized sub-5 nm-sized 1T′-$ReSe_2$ nanoflakes on carbon nanotubes and attained a significantly boosted HER activity with the overpotentials at 1 and 10 mA cm^{-2} being only 23 and 60 mV, the Tafel slope 37 mV dec^{-1}, and the exchange current density 0.3 mA cm^{-2}.

3.3 Role of Strains and vacancies

In addition to phase and composition, strains and vacancies in TMDs are another two vital factors that could significantly influence their HER behaviors [67]. Strains in TMDs can reduce the energy need for 2H to 1T/1T′ phase transition and modulate hydrogen adsorption and desorption [94, 100]. The large concentration of locally strained bonds contributed greatly to the stabilization of the 1T-WS_2 and promoted the HER activity [58]. The ΔG_{H*} on a strain-free chemically exfoliated 1T-WS_2 is calculated to be 0.28 eV. After the introduction of 2%–3% tensile strain, the ΔG_{H*} was close to zero as the tensile strain enhanced the density of states near the Fermi level (Fig. 3b) [57, 58]. Besides, it was demonstrated on 1T-MoS_2 theoretically that the biaxial tensile strain could induce the change of ΔG_{H*} more dramatically than the uniaxial one (Fig. 3c) [101]. However, the compressive strain would make ΔG_{H*} on 1T-MoS_2 and 1T-NbS_2 further away from zero and deteriorate HER performance.

Based on the in-depth understanding of strain engineering, stable and efficient 1T TMDs catalysts can be rationally designed at the interface of two materials. Shang et al. [102] constructed an ultra-stable 1T-MoS_2 at the contact areas between Pd nanosheets with a single-side-nucleated (SSN) Au nanoisland and 2H-MoS_2. The lattice mismatch and accordingly covalent bonds at the interface not only generated a compressive strain to trigger the phase transition but also stabilized the resulting 1T structure. The obtained SSN-Au/Pd-MoS_2 showed ideal phenomena toward HER with an onset potential of nearly 0 mV and a small Tafel slope of

49 mV dec^{-1} under light illumination. Likewise, mechanical curvature strain and interfacial-chemical interaction contributed to the formation of stable 1T cobalt-doped WSe_2 on the surface of carbon nanotubes [103]. Moreover, the variation in the curvature could increase the 1T-phase concentration from 67.2% to 82.9%, most of which could be maintained even after high-temperature annealing.

Defective sites are essential in promoting the HER activities of most TMDs. S vacancies are important catalytically active sites for 1T-MoS_2 [67]. The defects created the vacancy or adsorption of different elements in different types of phases could play distinctive roles. For instance, first-principle calculation investigation by Zhang et al. [85] on the intrinsic defects in basal planes of monolayer VS_2 toward HER suggested that the S_{ad}, S_{vac}, V_{ad}, and V_S of 2H-VS_2 and S_{ad}, S_{vac}, and V_{ad} of 1T-VS_2 were stable defects. Among them, S_{vac}, V_{ad}, and V_S in the 2H phase and V_{ad} in the 1T phase contributed to the HER activity.

Generally, two types of defects are most observed in 1T TMDs. The in-plane ones can be directly generated by oxygen plasma [86], ion beam [104], electron etching [105], or by heteroatom doping like Co, Ni, O, etc. [106–108]. The other is grain boundary, which can be maximized at nanosized and few-layer TMDs [109]. Precise control of defects can achieve significant electronic modulations. In a Ru-doped MoS_2, the proximal sites of Ru atom are energetically favorable to form V_S. The doped Ru atoms and subsequent V_S brought synergistic effects in reducing the $\Delta G(H_2O)$ and ΔG_{H*} [106]. The same phenomena were observed in Co–O-1T-MoS_2/SWNT and NiO@1T-MoS_2 catalysts as well [107, 108].

In a certain range, the number of HER active sites and thus the HER activity could increase promotionally with the increased number of defects. Typically, Zhang et al.[71] created 1D or quasi-2D defects precisely and quantitatively on the 200 μm × 200 μm region of the few-layer 1T-$MoTe_2$ film with a focused ion beam. With either the 200 μm × 1 μm linear defects increased from 5 to 40 or the 5 μm hole defects from 5 × 5 to 15 × 15, a continuous decrease of η_{10} and the Tafel slope were observed. The 2D defects with electrons moving freely in all directions overwhelmed the 1D defects with linear electrons transport. At optimal conditions, nanoporous 1T-$MoTe_2$ film achieved the current density of 100 mA cm^{-2} at an overpotential of −296 mV with a record-low Tafel slope of 44 mV dec^{-1}.

4 Strategies for Phase and Morphology Control

Due to the multiple polymorphs of TMD materials, strategies in controlling their phases are essential to obtain TMDs with desirable properties. Meanwhile, since the morphology of a TMD, which considerably affects HER performance, could change during its phase transition, morphology tuning during the phase engineering process should be considered. Up to now, a bunch of methods have been developed for synthesizing 1T/1T′ TMDs [38, 39]. Herein, these methods will be briefly introduced with an emphasis on the recent progress.

4.1 Chemical Exfoliation

The conversion of 2H bulk group 6 TMDs to their 1T/1T′ counterpart is mostly achieved by chemical exfoliation when the significance of 1T TMDs for HER was just realized [57, 58, 63]. Organic n-butyl lithium exfoliation, which consists of the preliminary lithium intercalation and forced hydration, is the most well-known and widely adopted approach for the 2H-1T phase transition in TMDs [38]. However, the low efficiency of lithiation (> 2 days), the extremely inert environment for stirring, and the violent reaction between lithium and water in the conventional intercalation exfoliation process make it difficult to control the morphology, size, and a 1T phase fraction of the exfoliated TMDs. Besides alkali metal compounds, surfactants, such as nonionic pluronic surfactant F108 with a molecular weight of ~ 14.6 kDa (F108, HO-$(C_2H_4O)_{141}(C_3H_6O)_{44}(C_2H_4O)_{141}H$) have also been successfully used to realize the exfoliation and conversion of WS_2 flakes into WS_2 nanodots with > 80% 1T phase [110]. Also, hydrogenation-induced phase transition, with hydrogen as the intercalating molecule, has been investigated by Qu et al. [111] on 33 different MX_2 monolayers.

Recently, Sofer and coworkers revealed that the concentration and stabilization degree of the 1T phase in TMDs are highly related to the properties of the interacted cations. While the cations of Li, Na, K, Ru, and Cs all could intercalate into MoS_2 and WS_2 and induce charge transfer from their naphtalenides to the sulfides surface, the smaller cations (e.g., Li^+ and Na^+) stabilized a large number of negative charges and induced high concentrations of the 1T phase [112]. This is because after exfoliation of the sulfides, the alkali metals were de-intercalated, and the negative charges on MoS_2 and WS_2 had to be compensated by protons in the water bilayer surrounding the sheets. The more prominent degree of hydrolysis with smaller cations (higher charge-to-radius ratio) allows the generation of more protons to stabilize the negative charges and 1T phases.

However, the conventional chemical exfoliation method is not applicable for $MoTe_2$ because that the strong layer-to-layer (van der Waals) interaction generated by the heavy tellurium (Te) atoms in $MoTe_2$ inhibits the effective insertion of alkali metal ions into the $MoTe_2$ during the chemical intercalation process. Recently, Yang and coworkers reported a convection-assisted lithium-ion (Li^+) intercalation method for converting the top and bottom surfaces of a 2H $MoTe_2$

crystal into 1T' structure [72]. The 1T'/2H/1T' vertical heterophase $MoTe_2$ exhibited efficient charge transfer with low contact resistance and abundant catalytic active sites. Besides, based on the unique vertical heterophase structure with weakened adhesion between the intercalated top layers, large-size 1T′ monolayers can be easily obtained by taking advantage of the surface tension of water droplets.

4.2 Electrochemical Exfoliation

With the introduction of additional voltage to control the intercalation process, electrochemical exfoliation is an upgraded alternative to the general chemical intercalation method for 2H → 1T phase conversion of TMDs [113]. With bipolar electrodes, WS_2 in the Na_2SO_4 solution was directly exfoliated and converted to 1T WS_2 nanosheets by applying 10 V DC potential across two Pt electrodes for 30 min [114]. In a three-electrode system, lithium intercalation into the interlayer of MoS_2 could occur with a $LiClO_4$ electrolyte and a driving force of −4.5 V for 2 h [115]. The obtained 1T MoS_2 showed a HER activity with an η_{10} of 0.13 V and a Tafel slope of 49 mV dec^{-1}.

By controlling the lithiation degree, the morphology of obtained 1T MoS_2 could be effectively tuned. Typically, Chen et al. [116] utilized an electrochemical cell with a MoS_2 cathode and a Li foil anode and operated it at a cut-off voltage of 0.7 V vs. Li^+/Li, which ensured an efficient phase transition with the reduction reaction of $MoS_2 \rightarrow [MoS_2]^{n-}$ (above −2.4 V vs. NHE) and avoided the decomposition of Li_xMoS_2 under deeper lithiation. A small x value was obtained at a fast-charging with a rate up to 1 A g^{-1} with lithiation taking place only in the peripheral part of MoS_2, producing MoS_2 nanosheets with a large mean lateral size (ca. 32.5 nm) and a wide lateral size distribution (ca. ± 11.9 nm). When the discharging rate decreased to 0.001 A g^{-1}, a full lithiation of MoS_2 in both the peripheral and the central parts could be achieved with MoS_2 splitting into small monolayer pieces (Fig. 4a). 1T MoS_2 quantum dots (QDs) was formed when the molar ratio of Li/M was 2. With the high 1T fraction up to 92%–97% and a small lateral size of about 3.0–4.5 nm, the 1T MoS_2 QDs are favorable for HER with an η_{10} of 92 mV, a Tafel slope of 44 mV dec^{-1}, and a j_0 of 4.16×10^{-4} A cm^{-2}.

Besides, recently, Wei and coworkers used a plasma-induced electrochemical method to exfoliate bulk MoS_2 (Fig. 4b) [117]. With a high voltage of 95 V applied across the tungsten rod cathode and the platinum foil anode in 2 M H_2SO_4 electrolytes, plasma jets were generated at the cathode and caused the exfoliation of lamellar MoS_2 particles. The exfoliated MoS_2 was subsequently combined with exfoliated graphene sheets under applied voltage

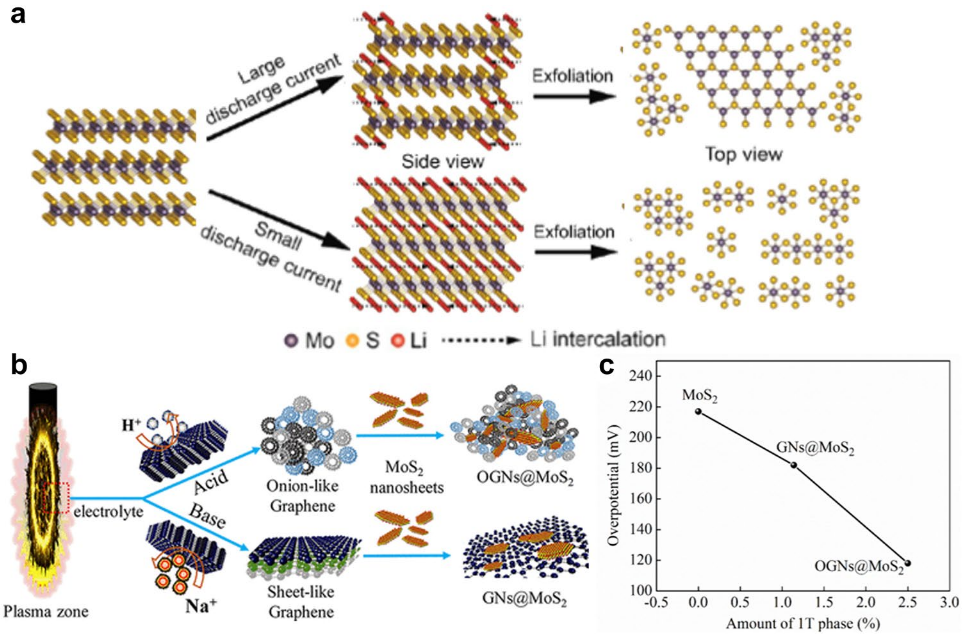

Fig. 4 **a** The large discharge current density induces partial intercalation and results in large lateral size and non-uniform phase distribution of 2D MoS_2 sheets and the small discharge current density induces full intercalation and results in small lateral size and uniform phase distribution of the 2D MoS_2 sheets. Reproduced with permission from Ref. [116]. Copyright 2018, American Chemical Society. **b** Schematic representation of the proposed mechanism of OGNs@MoS_2 and GNs@MoS_2. **c** Relationship between total amount of the MoS_2 1T phase and overpotential at current density of 10 mA cm^{-2} of MoS_2, GNs@MoS_2, and OGNs@MoS_2. Reproduced with permission from Ref. [117]. Copyright 2020, American Chemical Society

(85 V) to form onion-like graphene nanosheets covered MoS_2 (OGNs@MoS_2) in 2 M H_2SO_4 electrolytes or sheet-like graphene-wrapped MoS_2 composite (GNs@MoS_2) in 2 M NaOH electrolyte. The marginal increase in the 1T phase among MoS_2 (0%), GNs@MoS_2 (1.14%), and OGNs@MoS_2 (2.5%) rendered a significant decrease in overpotential for HER (Fig. 4c). Nevertheless, the method can be improved to increase the overall 1T percentage in the product.

4.3 Anion Extraction Induced Phase Transition

Apart from chemical intercalation, anion extraction has recently been revealed as an efficient strategy to induce the 2H to 1T (1T′) phase transition. Principally, the transition relies on the formation of chalcogen vacancies, which can be regarded as another type of electron donors to promote the phase transition, generate extra charges, and weaken the metal–chalcogen bonds. In contrast to the 2H phase with clustered defects, chalcogen vacancies in the 1T counterpart tend to be isolated at low concentrations and linearly organized at high concentrations. Based on Tang et al.'s [118] work, the appearance of chalcogen vacancies reduced the energy barrier between 2H and 1T (1T′) phases. When the chalcogen defects reached the critical concentration (i.e., 22% for MoS_2, 20% for $MoSe_2$, and 4% for $MoTe_2$), the 1T (1T′) phase became more stable than the 2H one. Meanwhile, Patra et al. [119] combined machine learning and molecular dynamics simulations with HRTEM to elucidate the defect-driven phase transition holistically. Using MoS_2 as a TMD model, the intriguing phase transition without intercalation species can be described by three continuous steps: (i) the formation of extended line defects through the migration and coalescence of site defects over seconds and minutes, (ii) rapid 2H to α-phase transition in the vicinity of line defects about ten picoseconds, and (iii) α-phase to 1T phase transformation within ~ 1 ns.

Although S extraction could be realized with the generation of S vacancies by exposing 2H TMDs to argon plasma treatment or electrochemical desulfurization, a substantial phase transition to 1T could hardly be achieved with the chalcogen vacancies merely appearing on the monolayers surface or accompanied by large amounts of incorporated oxygen [120, 121]. Innovatively, Joo and coworkers designed an anion-extracted MoS_2 with a 1T percentage up to 58%, taking advantage of the selective reaction between CO and chalcogen atoms, i.e., $MoS_2 + \delta \cdot CO(g) \rightarrow MoS_{2-\delta} + \delta \cdot COS(g)$ (Fig. 5a) [122]. The formed sulfur vacancies (V_S) induced the S coordination from hexagonal to octahedral one. The solid–gas reaction is favorable for polymorph control on a large scale. However, there is a large possibility to attain unexpected products (solids, like MoO_2, Mo_2C, MoC, and C, and gases, for example, SO_2 and CS_2) if the CO/CO_2 ratio and the mole fraction of MoS_2 were not precisely controlled. The 1T percentage in the anion-extracted MoS_2 should be precisely controlled by tuning the operation parameters (designed on the basis of the MoS_2-CO-CO_2 ternary

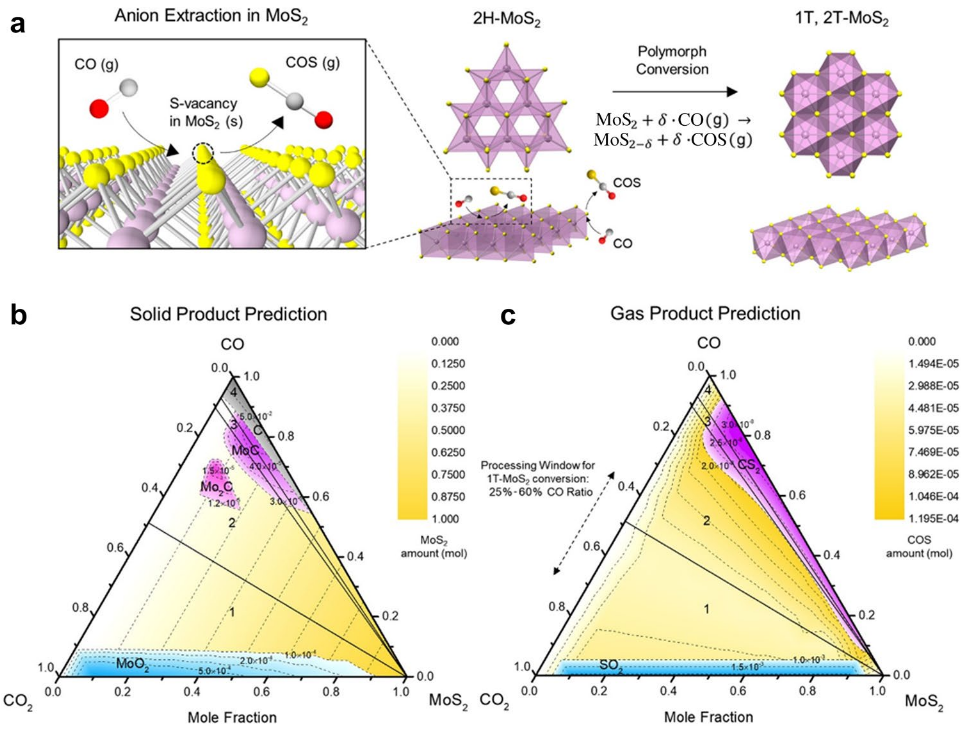

Fig. 5 **a** CO/CO_2 calcination-based MoS_2 polymorph control by selective reaction between MoS_2 and CO to form V_S; calculated ternary phase diagrams with **b** solid and **c** gas product distributions at 800 °C calcination to predict MoS_2, CO, and CO_2 mole fractions for 1T-MoS_2 formation. Reproduced with permission from Ref. [122]. Copyright 2019, American Chemical Society

phase diagram, Fig. 5b, c) and by varying the stacking layer number and length of the MoS_2 precursor. The processing window for the formation of merely COS and V_S was associated with 25%–60% CO. The best HER activity (an overpotential as low as 80.5 mV at 10 mA cm^{-2} and a Tafel slope of 38.2 mV dec^{-1}) was achieved with MoS_2/CNTs fabricated in a 40% CO atmosphere at 800 °C for 5 h.

4.4 Mechanical Exfoliation and Shape Control

Mechanical approaches like scotch-tape micromechanical cleavage [123] and solvent-assisted sonication [124] are effective for preparing single- or few-layer TMDs. The mechanical forces are efficacious in controlling the phase and morphology of TMDs as well. Ball milling can be exploited to get micro-sized TMDs crystals, which is an intermediate to fabricate 1T TMDs dots [125]. Hu and coworkers demonstrated that the 2H-to-1T phase transition could be attained by ball milling and the 1T percentage (from 8 to 20%) increased with the prolonged milling time (from 2 to 10 h) [24]. Similarly, bulk TiS_2 crystals were first exfoliated into few-layer nanosheets by bath sonication and then incised into 1T TiS_2 QDs by probe sonication in acetonitrile/isopropyl alcohol (MeCN/IPA) cosolvent at room temperature [82]. The surface tensions of TiS_2, MeCN, and IPA contributed to the 1T phase conversion, which particularly occurred at a volume ratio of 19:1 for MeCN/IPA. The as-obtained TiS_2 QDs with a uniform lateral size of 3–6 nm and atomic layer thickness of 1–2 nm demonstrated an excellent HER activity, surpassing those of TiS_2 nanosheets and MoS_2 QDs prepared by the same method.

4.5 Wet Chemical Synthesis

Compared to the aforementioned top-down methods for obtaining 1T TMDs, several bottom-up strategies that show the advances in manipulating the morphology of 1T TMDs have been explored [126]. 1T′ phase-dominated nanoparticle-like WS_2 (1T′-D WS_2), consisting of closely stacked thin nanosheets, was synthesized by a one-pot colloid chemistry. In this process, 0.2 mmol $(NH_4)_2WO_4$ reacted with 0.6 mmol thiourea and 20 mmol surfactants at 280 °C for 90 min [127]. The combination of surfactants (OM: oleylamine and OA: oleic acid) tuned the phase structure by their electrostatic interaction with the surface charges of $[WS_2]^{n-}$. 1T′-WS_2 was produced by solely using OM, and the 1T′-WS_2 gradually changed to 2H-WS_2 by adding a small amount of OA. Except for closely stacked 1T′-WS_2 nanosheets, metallic-phase MoS_2 nanopetals [128] and nanoflowers [129] were constructed by hydrothermal reactions.

During the hydrothermal synthesis process, a large molar ratio (x) of the reductant ($NaBH_4$, etc.) to the Mo precursor (e.g., $NH_4MoO_4 \cdot 2H_2O$) was favorable for the conversion of the 2H → 1T phase because the excessive amount of reductant induced the rearrangement of the atomic and electronic structure [130]. Meanwhile, the reaction temperature T should be carefully controlled as a higher T would lower the disorders and reduce the ratio of the 1T phase. Taking both factors into account, $MoSe_2$ obtained at $x=4$ and $T=180$ °C showed a 55% 1T phase and the best HER performance (an η_{10} of 152 mV and a Tafel slope of 52 mV dec^{-1}).

4.6 Chemical Vapor Deposition

Chemical vapor deposition (CVD) methods have been particularly applied for the synthesis of stable 1T TMDs, like 1T-TaS_2, 1T-VS_2, etc. Compared to the lithiation approaches, the CVD method allows the formation of purer 1T phase for TMDs. Generally, the CVD growth is carried out on a planar substrate, with which the production is very limited. To allow a mass production of the TMDs, 3D templates are desirable. Recently, Huan et al. [87] have employed green, abundant, and soluble NaCl crystals as templates for atmospheric pressure CVD (APCVD) synthesis of high-quality 2D metallic TMDs (e.g., TaS_2, V_5S_8, and NbS_2) nanosheets. Representatively, 1T-TaS_2 flakes with uniform thickness and domain size were successfully formed at the edges, corners, and surfaces of the 3D NaCl crystals. After the CVD process, high-quality 1T-TaS_2 powders were resulted by facilely dissolving the NaCl templates in water.

5 Advanced 1T TMD-Based Materials for Efficient and Durable HER

An ideal HER catalyst should not only be efficient but also be electrochemically stable [56]. One significant issue of 1T TMDs, especially the 1T structures of group 6 TMDs, is their gradual transition to more stable phases during cycling utilization. Thereby, a series of advanced 1T TMD-based materials have been attempted in the past few years to achieve an efficient and durable hydrogen production.

5.1 Charge Mediated 1T TMDs

Mediating the charges on TMDs surface could not only lead to the phase transition between 2H and 1T/1T′ but also enhance the stability of the 1T/1T′ structures. DFT calculation showed the injection of $4e^-$ into the MoS_2 unit can lower the kinetic energy barriers of phase transition from 1.59 to 0.27 eV and increase the thermodynamic stability of 1T-MoS_2 (Fig. 6a) [131]. Metal cation intercalation, non-metal doping, and surface organic functionalization are three effective routes in mediating the charges on TMDs and stabilizing the 1T phase. As a special form of doping, the

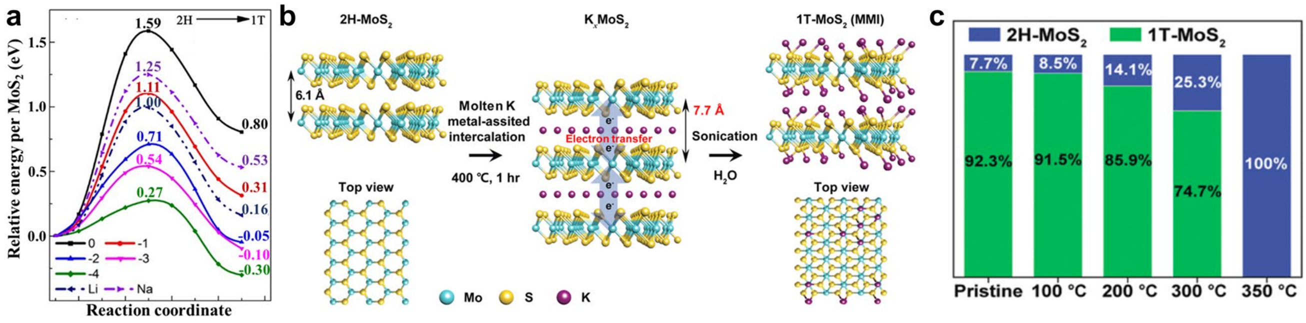

Fig. 6 **a** Minimum energy pathways of phase transition from 2H to 1T in different charge states or with ions intercalation. Reproduced with permission from Ref. [131]. Copyright 2015, American Chemical Society. **b** Synthesis of 1T-MoS$_2$ via the molten-metal-assisted intercalation (MMI) approach; **c** relative fraction of 1T and 2H phase as a function of annealing temperature. Reproduced with permission from Ref. [132]. Copyright 2020, John Wiley and Sons

construction of 1T TMD alloys allows the mediation and stabilization of the surface charges as well.

5.1.1 Cation Intercalation

Intercalation of several metal cations, including K [132], Ca, Co [133], Rh [134], V, Nb, Ta [135], Pb [136], and Cu [137], has been proven effective in realizing the charge injection into and stabilizing the metastable phases. Typically, 1T MoS$_2$ with 92% phase purity and doped potassium was recently prepared by molten-metal-assisted intercalation (MMI) (Fig. 6b) [132]. K can play a dominant role in the 2H-to-1T phase transition. As revealed by DFT calculation, K doping decreases the request heat for the reaction of phase transition without significant influence on the reaction pathway. Higher K content in K$_x$MoS$_2$ allows the endothermic reaction to being exothermic and metastable 1T structure stabilized. Moreover, K that resided near the S forms a K-S ionic bonding, which can facilitate the electron transfer and suppress electron emission. Impressively, thanks to this doping effect, the 1T phase was extremely stable, maintaining a 1T fraction up to 74.7% upon annealing at 300 °C (Fig. 6c) and showing no conceivable degradation within 5000

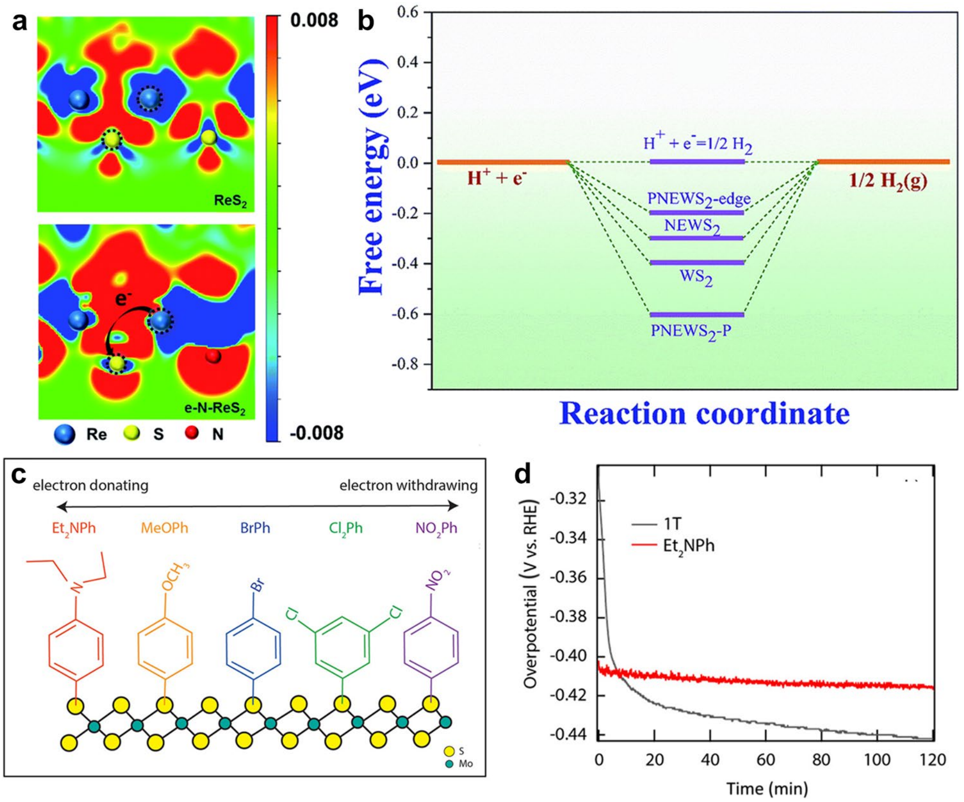

Fig. 7 **a** The charge density differences between e-ReS$_2$ and e-N-ReS$_2$. The blue, yellow, red, green and white spheres represent Re, S, N, O, and H atoms. Reproduced with permission from Ref. [139]. Copyright 2020, The Royal Society of Chemistry. **b** Free energy diagram of WS$_2$, NEWS$_2$, PNEWS$_2$-P site and PNEWS$_2$-edge. Reproduced with permission from Ref. [141]. Copyright 2018, The Royal Society of Chemistry. **c** Schematic of the various functional groups on 1T MoS$_2$. **d** Overpotential is measured as a function of time to maintain a current density of 10 mA cm^{-2}. Et$_2$NPh outperforms 1T-MoS$_2$ for H$_2$ generation within ~ 7 min. Reproduced with permission from Ref. [142]. Copyright 2018, American Chemical Society

consecutive CV scans in either acidic or alkaline electrolyte during HER.

5.1.2 Non-metal Doping

Oxygen incorporation into the 1T-WS_2 lattice can improve the conductivity with its j_0 (2.2×10^{-2} mA cm^{-2}) two times larger than that of 1T nanoclusters [138]. The obtained 1T-WS_2 is nanosized, edge-tailed, and oxygen-incorporated (O-WS_2-1T) with an η_{10} of 88 mV and an Tafel slope of 47 mV dec^{-1} for HER. The superior performance could last for at least 500 h, exceeding those of its 2H counterpart (O-WS_2-2H) and the ball-milled WS_2 with 1T phase (BM-WS_2-1T). Apart from oxygen, N implantation into MX_2 could induce electron transfer from M to X atoms (Fig. 7a). The electron redistribution can facilitate H_2 generation as the electron-deficient M atoms enhance the O affinity for the capture and activation of H_2O, and the electron-accumulated X atoms strengthen the H adsorption. Also, N implantation accelerates charge transfer in MX_2 because N atom attracts more extra electrons (about 0.853 electrons) and increases electronic states near the Fermi energy level. Thus, 9.67 at.% N implanted ReS_2 grown on carbon cloth (N-ReS_2-6/CC) showed stable HER activity for 140 h in 1 M KOH with a low η_{10} of 90 mV [139].

The doping level of N can be tuned by alkyl amines with different atomic numbers (1–4) [140]. In a hydrothermally synthesized 1T′-MoS_2 (MS), doping of amine molecules could reach 10 at.% in MS-4. The accumulated N and 160% lattice expansion in MS contributed to a facilitated HER with an $\eta_{10}=0.16$ V and Tafel slope = 36 mV dec^{-1}. Compared with nitrogen-doped WS_2 (NEWS_2), nitrogen- and phosphorus-codoped WS_2 (PNEWS_2) showed even less negative ΔG_{H*} and higher electrochemically active surface area ($C_{dl}=37.1$ mF cm^{-2}) [141]. Resultantly, PNEWS_2 catalyst displayed more efficient hydrogen evolution with a low overpotential of 59 mV, a small Tafel slope of 35 mV dec^{-1}, large TOF of 0.7 s^{-1}, high exchange current density of 1.15 mA cm^{-2} and high stability in a 15-h test (Fig. 7b).

5.1.3 Organic Functionalization

As suggested by Miller and coworkers, the electronic properties and accordingly the HER performance of 1T-MoS_2 could be modified via covalent chemical functionalization by organic phenyl rings containing electron-donating or withdrawing groups (Fig. 7c) [142]. Comparatively, the electron-donating groups show a stronger ability in reducing the overpotential and the Tafel slope for HER. Specifically, while the unmodified 1T-MoS_2 presented a dramatically degrading HER activity within 10 min, the 1T-MoS_2 modified by the most electron-donating functional group (Et_2NPh) showed only a slight degradation within 2 h (Fig. 7d). This was because the extra charges on 1T-Et_2NPh-MoS_2 separated the thermodynamic barrier of 1T and 2H phases and tuned the surface energetics close to the thermoneutral. Thus, 1T-Et_2NPh-MoS_2, as an efficient catalyst, showed advantages in long-term hydrogen production. Besides, first-principle calculation indicated that the strong adsorption of –H, –O, –SH, –NH_2, –CH_3, –CF_3, –SCH_3, and –OCH_3 on 1T TMDs induced the transformation of the 1T phase to the more stable 1T′ phase [143].

5.1.4 Alloying Effect

Alloying, which substitutes metal or chalcogen atoms in the parent TMDs, would tailor the phase transition and the catalytic stability of 1T TMDs [125, 144, 145]. The significant role of chalcogen alloying was demonstrated by Tan et al. [125] when comparing the catalytic activity of MoS_2, WS_2, $MoSe_2$, $Mo_{0.5}W_{0.5}S_2$, and MoSSe. Bulk TMDs materials were broken into small pieces via ball milling, and the following Li-chemical exfoliation realized the efficient 2H-1T phase transition and the single-layer structure. Although all these 1T TMD dots showed rich active edge sites, high electrical conductivities, and HER activities better than that of the corresponding 1T nanosheets, 1T-MoSSe nanodots achieved the most efficient H_2 production with an η_{10} at 140 mV, a Tafel slope of 40 mV dec^{-1} and a high stability in continuous 10000 cycling tests. The enhanced HER activity of 1T-MoSSe dots was attributed to the negative surface charge (zeta potential up to 41.6 eV), high 1T fraction up to 71%, single-layer structure (9 Å), ultra-small size of the 3–5 nm. More importantly, the alloying of S and Se at the basal planes, which yielded excess electrons around Se vacancies and decreased the ΔG_{H*} to 0.19 V, stabilized the 1T structure during continuous hydrogen production. Likewise, the electronic modulation at the heterointerface of the coupled Mo-Fe selenide promoted HER performance. As a result of the metal alloying effect, the electrons transferred from $FeSe_2$ to the active edges of 1T-$MoSe_2$ [145]. During HER in acidic solution, the Mo-Fe heterostructure on carbon paper (Mo-Fe(1/1)-Se-CP) only required an overpotential of 86.9 mV to achieve a current density of 10 mA cm^{-2} with a Tafel slope of 57.7 mV dec^{-1}. It also showed a high stability with an 8.4% increase in η_{10} after 22 h (compared to the value obtained in 2 h), much lower than 11.3%, and 13.7% for $MoSe_2$-CP and $FeSe_2$-CP, respectively.

Generally, a TMD alloy shows site-specific activity with the different composing elements playing different roles. When the Re/(Re + Mo) concentration was larger than 50%, ReMoS_2 would achieve an energetically favorable transition from 2H to stable distorted tetragonal (DT)

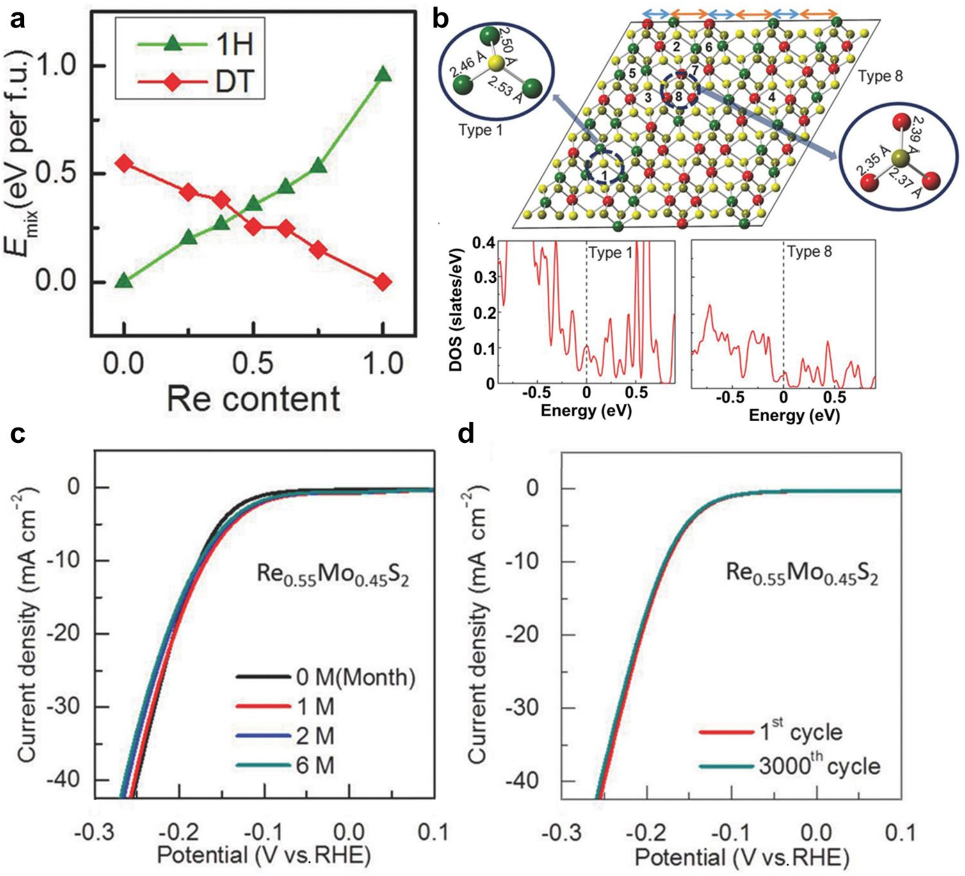

Fig. 8 **a** Calculated mixing energy in 1H and DT (1T′) phase $Re_xMo_{1-x}S_2$ alloy at different Re concentrations; **b** structural model of a DT (1T′) phase $Re_xMo_{1-x}S_2$ alloy monolayer with randomly distributed Re atoms and the projected DOS of the most active (Type 1) and the least active sites (Type 8), respectively. Mo atoms in green, Re atoms in red, and S atoms in yellow. The strings and channels are identified with blue and orange arrows, respectively. S atom bonded with three Mo atoms in between two metal rhombic strings (zoomed-in view of Type 1) serves as the most active site, while S bonded with three Re atoms within the metal strings (zoomed-in view of Type 8) is the least active site; Stability test of $Re_{0.55}Mo_{0.45}S_2$ alloy and 1T-MoS_2 over time and cycling: polarization curves measured after **c** 1, 2, and 6 months of storage in air under ambient conditions and **d** for the first cycle and 3000th cycle. Reproduced with permission from Ref. [146]. Copyright 2018, John Wiley and Sons

phase (Fig. 8a) [146]. In such a $ReMoS_2$, the most active sites ($\Delta G_H = 0.06$ eV) were the S sites surrounded by three Mo atoms (the longest Mo-S bonds), and the least active sites ($\Delta G_H = 1.36$ eV) were the S sites surrounded by three Re atoms (the longest Re–S bonds) (Fig. 8b). It suggests that the Mo-rich 1T phase was the primary active site, while the Re intercalation stabilized the 1T structure. As a result, the optimal HER performance was achieved in 55% Re-45% Mo (Re, Mo)S_2 alloy ($Re_{0.55}Mo_{0.45}S_2$) with an η_{10} of 90 mV, a Tafel slope of 56 mV dec^{-1}, and TOF of 3.48 s^{-1} (at $\eta = 300$ mV) and 0.015 s^{-1} (at $\eta = 0$ mV). The H_2 yield of $Re_{0.55}Mo_{0.45}S_2$ was stable, with only 5% increase of η_{10} after 6-month air storage (Fig. 8c) and a slight increment of η_{10} (2 mV) after 3000 cycles (Fig. 8d). Except for isoelectronic substitutions, stable 1T TMDs alloy can also be non-isoelectronic substitutions.

Defects and strains are readily associated with the lattice mismatch and interfacial stress in TMD alloys obtained by either anion doping ($WSe_{2x}S_{2-2x}$) or cation doping ($W_xMo_{1-x}S_2$ and $W_xMo_{1-x}Se_2$) [97]. Thanks to the synergistic effect among its porous structure, 1T phase, and defects, strained $W(Se_xS_{1-x})_2$ exhibited an excellent HER activity with an η_{10} of 110 mV and a Tafel slope of 59 dec^{-1} and appreciable stability (kept constant at 10 mA cm^{-2} for 30 000 s) [147].

5.2 1T/2H Mixed Phases

The pure 1T TMD structures are intriguing with its excellent properties for HER. However, the synthesis of the metastable 1T polymorph requires intensive chemical exfoliation or delicate fabrication control. As an alternative, 1T/2H multiphase structures, which are relatively stable and outperform their 2H counterparts in HER, have been prepared by facile synthesis routes, represented by hydrothermal approach. There are two primary forms of 1T/2H heterostructures, i.e., in-plane and out-of-plane 1T/2H structure.

5.2.1 In-Plane 1T/2H Phases

The in-plane 1T/2H TMDs are with 1T domains grown in 2H planes. Compared to the complete 2H structure, they possess additional active sites, improved conductivity, and thereby advanced HER performance. Moreover, with an

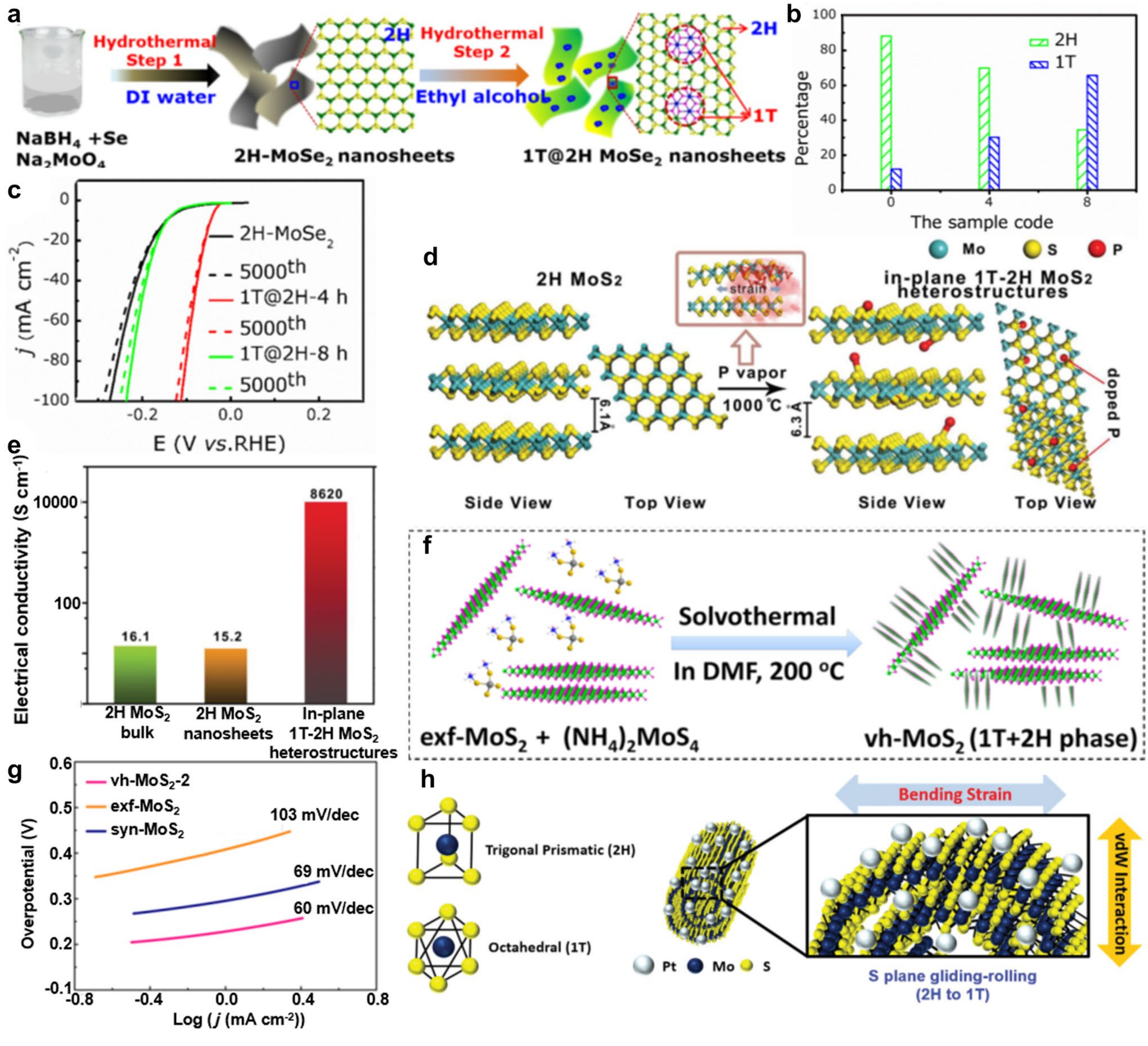

Fig. 9 **a** Schematic representation of the two-step hydrothermal synthetic route for the 1T@2H-MoSe$_2$ nanosheets; **b** extracted relative fraction of 1T and 2H components from XPS analysis; **c** durability test for the catalysts of 2H-MoSe$_2$, 1T@2H-MoSe$_2$-4, 1T@2H-MoSe$_2$-8 nanosheets. Reproduced with permission from Ref. [151]. Copyright 2016, Elsevier. **d** Schematic for the partial phase transition process of semiconducting 2H-MoS$_2$ to metallic 1T-MoS$_2$ induced by phosphorus atoms; **e** electrical conductivity of in-plane 1T-2H-MoS$_2$ heterostructures compared with 2H MoS$_2$ bulk and nanosheets. Reproduced with permission from Ref. [154]. Copyright 2018, John Wiley and Sons. **f** Schematic solvothermal synthesis of vh-MoS$_2$ in the presence of exf-MoS$_2$ nanosheets; **g** the corresponding Tafel plots from the polarization curves at a scan rate of 0.5 mV s^{-1} for exf-MoS$_2$, syn-MoS$_2$, and vh-MoS$_2$. Reproduced with permission from Ref. [155]. Copyright 2016, American Chemical Society. **h** Schematic models of 2H and 1T MoS$_2$ structure and cross-sectional views of MoS$_2$@Pt scrolls with the bending strain stabilized by van der Waals interactions. Reproduced with permission from Ref. [157]. Copyright 2017, The Royal Society of Chemistry

in-plane structure, the misfit lattices between 2H and 1T nanodomains yield amorphous regions and defects, which could partially release the lattice stress and stabilize the 1T phase. These in-plane 1T/2H TMDs can be prepared via a one-step hydrothermal synthesis with the presence of propionic acid [148] or via proper control of the reaction condition [149]. The in situ generation of the 72% 1T phase in a 2H-MoS_2 with the aid of propionic acid was supposed to proceed via the formation of a key intermediate species, [MoO_6], based on a reduction-first hypothesis [148]. The obtained 1T/2H-MoS_2 exhibited a stable H_2 production over 1000 LSV scans and a 10-h chronoamperometry test. Even after 30 days of air-contact, the 1T/2H-MoS_2 afforded considerably retained activity.

Alternatively, hydrothermally obtained a 2H phase TMD can be partially transformed into the corresponding 1T structure in a second hydrothermal process with the assistance of ethanol and high temperature (Fig. 9a) [150, 151]. The 1T@2H-$MoSe_2$ obtained after 4-h reaction (1T@2H-$MoSe_2$-4), which showed a medium ratio of 1T phase (Fig. 9b) but a high level of electron concentration and active sites, presented the lowest onset potential of 20 mV and the smallest b of 41 mV dec^{-1} (Fig. 9c) [151]. The high H_2 production could keep stable for 5000 LSV scans and a 10-h chronoamperometry test. Besides, the intercalation of guest ions and molecules can induce the in situ phase transition from 2H to 1T [152, 153]. In a reverse-micelle-induced microemulsion process, supercritical CO_2 molecules entered PVP-modified MoS_2 interlayers and generated swollen CO_2 domains [153]. Subsequently, the expansion of the micelles and decreased interlayer interaction reversed the micelles from CO_2-in-water emulsions to water-in-CO_2 emulsions. The strain in the curvature transition resulted in a 90% 1T phase in single-layer MoS_2. Furthermore, as red phosphorous vapor was gradually inserted into interlayers of MoS_2 bulk crystals, it not only broadened the interlayer distance to 0.63 nm but also was embedded into the S-Mo-S atomic planes [154]. The glide of the S atomic planes around the P-doped regions led to the generation of in-plane 1T domains (Fig. 9d) [154]. Resultantly, the in-plane 1T-2H MoS_2 attained a high electrical conductivity up to 8620 S m^{-1}, 500 times higher than that of pristine 2H MoS_2, and a large electrochemically active surface area of 60.3 cm^2 (Fig. 9e), along with a good HER activity that showed an η of 320 mV at a high current density of 20 mA cm^{-2}, a Tafel slope of 65 mV dec^{-1}, and appreciable stability in 1000 cycles.

5.2.2 Out-of-Plane 1T/2H Phases

The out-of-plane 1T/2H heterostructures are the composites of 1T nanosheets and 2H structures. With the presence of 1T lattice on a 2H base, the surface property of the original materials can be dramatically altered: the ΔG_{H*} could be remarkably closer to zero, and a higher edge/basal ratio and an improved conductivity would be obtained. Typically, with ammonium thiomolybdate as a precursor, an ultrathin, interconnected, and wrinkled syn-MoS_2 (vertically grown 1T-MoS_2) was uniformly and vertically grown on large-lateral exfoliated 2H-MoS_2 (exf-MoS_2) (Fig. 9f) [155]. The syn-MoS_2 possessed an edge-to-edge configuration with rich active sites, well-defined interior voids, and a large surface area. Meanwhile, the coexistence of 2H and 1T phases with high conductivity and the continuous structure supported rapid electron transfer. Thus, an excellent performance for hydrogen evolution was achieved with an η_{10} of 203 mV, a Tafel slope of 60 mV dec^{-1}, and 5000-time stable cycling (Fig. 9g). Similarly, out-of-plane CoSe/$MoSe_2$ heterostructure also achieved highly efficient and stable HER performance [156]. Besides, in MoS_2@Pt scroll, rolling up of 2H-MoS_2 sheets achieved a hybrid 1T/2H structure with 1T phase up to 28% (Fig. 9h) [157]. This 2H-to-1T phase transition was initiated by the bending strain (2.4%), which led to the gliding of the interlayer S-plane. The obtained 1T phase was stabilized by the van der Waals interactions between the layers. With 8.3 wt% Pt nanoparticles, the 1T/2H-MoS_2@Pt scrolls attained a ΔG_H close to 0 and a superb HER activity with a Tafel slope of 39 mV dec^{-1}. Similarly, 1T/2H-WS_2 with 70% 1T was grown vertically on the Ti structure by a hydrothermal approach [158]. The vertical growth and distortion (caused strain) of the sheets allowed the material to show a maximized number of active sites and high stability, respectively, during the HER process. As a result, a low overpotential of 118 mV at 10 mA cm^{-2} and a Tafel slope of 43 mV dec^{-1} were achieved on the 1T/2H WS_2, along with outstanding stability for 5000 continuous CV cycles.

5.3 1T TMD-Based Composite Materials

5.3.1 Hybrids of 1T TMDs and Conductive Supports

The incorporation of 1T TMDs with conducting supports (carbon or metal substances) can stabilize the 1T structures and improve the HER performance effectively. It takes advantage of both the high catalytic activity of 1T TMDs, the tunable surface, high conductivity, and stable chemical/electrochemical properties of the conducting supports, and their synergistic effects. The electron injection and lattice strain at the interfaces further contribute to the catalytic performance of the catalysts [32, 159]. Nowadays, the most widely applied conducting supports include metal substrates like Mo foil, Au foil, Au nanowire, etc. [160, 161], and carbon materials, like glassy carbon, carbon fibers [162], carbon cloth [163], carbon nanotubes (CNTs) [164], graphene [165], graphdiyne [166], carbon nanoflowers [167], graphite rods [149, 168], etc.

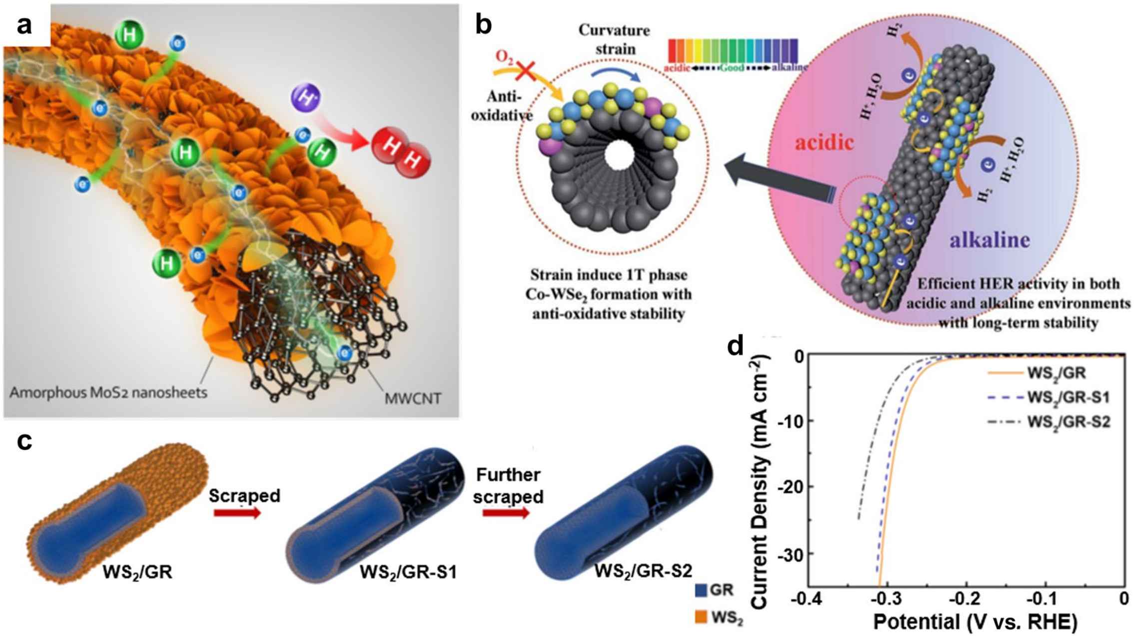

Fig. 10 **a** Schematic illustration of the mechanism governing the electrocatalytic HER on the MoS_2 NS/MWCNT structure. Reproduced with permission from Ref. [169]. Copyright 2017, Springer Nature. **b** HER scheme for the Co-WSe_2/MWNT heterostructure catalyst. Reproduced with permission from Ref. [171]. Copyright 2018, The Royal Society of Chemistry. **c** Schematic illustration of WS_2/GR, WS_2/GR-S1, and WS_2/GR-S2; (d) polarization curves of WS_2/GR, WS_2/GR-S1, and WS_2/GR-S2. Reproduced with permission from Ref. [168]. Copyright 2019, American Chemical Society

The interfacial engineering is important for maximizing the number of active sites and promoting the HER kinetics. Nanohybrids of 1T-MoS_2 nanosheets (NS) leaves and multiwall CNTs (MWCNTs) stems [169] and heterostructures of 1T-MoS_2 nanopatches and single-walled CNTs (1T-MoS_2/SWCNT) were successfully constructed by hydrothermal methods [170]. A proper content of CNTs in the composite materials could effectively avoid the aggregation of 1T-MoS_2 and allow their uniform dispersion with fully exposed catalytically active sites. The deformed charge density at the interfaces stimulated the electron transfer (0.924 electrons) spontaneously from the whole CNT surface to the upper 1T MoS_2 surface (Fig. 10a), which weakened the absorption energy of the H atom on electron-doped 1T-MoS_2 [169]. Due to this interfacial medication, both types of nanohybrids attained stable HER activities without noticeable degradation over thousands of cycles (2000 LSV cycles for MoS_2 NS/MWCNT and during 3000 LSV cycles for 1T-MoS_2/SWCNT) with a small onset potential and a low Tafel slope.

Additionally, the curvature strain of nanosized CNTs could affect the 1T content, morphology, and HER performance (Fig. 10b) [171]. The percentage of 1T phase WSe_2 was up to 72.1% in a strained cobalt-doped WSe_2/MWCNTs, which is higher than 60.0% in Co-WSe_2 and 58.7% in Co-WSe_2/rGO. Regarding rGO as a flat CNT, it is clear that curvature strain was responsible for the predominant 1T polymorph in Co-WSe_2/MWNTs. Besides, the metastable 1T phase was efficiently stabilized by the MWCNTs with a decreased oxidation degree from 58.6% to 32.3%. Therefore, high HER activity with long-term stability was achieved on the heterostructured catalyst over a wide PH range. Overpotentials of 174 mV and 241 mV were required to drive H_2 generation at the current density of 10 mA cm^{-2} in 0.5 M H_2SO_4 and 1 M KOH electrolytes, respectively. Except for CNTs, the nitrogen-doped vertical graphene (N-VG) can act as a substrate for the growth of wrinkled $MoSe_2$ nanoflakes [172]. The synergistic effects of doping, phase, and morphology contributed to the superior HER activity and stability of N-doped 1T/2H$MoSe_2$/VG (with η_{10} of 98 mV and a Tafel slope of 49 mV dec^{-1}) to those of $MoSe_2$/VG (with η_{10} of 190 mV and a Tafel slope of 62 mV dec^{-1}), N-VG (with η_{10} of 294 mV and a Tafel slope of 123 mV dec^{-1}), and VG (with an onset potential of 347 mV and a Tafel slope of 184 mV dec^{-1}).

Graphite rod (GR) is a special carbon substrate, which consists of plenty of slits and channels [149, 168]. When using a GR as the substrate for the growth of TMDs in order to build a binder-free free-standing electrode, the TMD materials can grow firmly on the inner surface of the rod, where the metastable phases could be protected from air and show high structural stability with in situ generated strains. For instance, 1T/2H-MoS_2 (with up to

62.8% of 1T) were uniformly grown on the GRs with compactly stacked MoS_2 ball flowers covered on the surface and MoS_2 nanoblanks filled in the interior pores and slits [149]. The intimate contact between MoS_2 and the substrate led to a charge transfer resistance as low as 1–5 Ω. The novel 3D electrodes obtained at 200 °C maintained its excellent HER performance even after 30-day storage due to protective effects of the GR to the hybrid-phase MoS_2. Attractively, when growing WS_2 on GRs [168], the disulfides formed at different positions of GRs contributed differently to HER. WS_2 nanosheets which occupied the pores and slits at the near-surface region dominated the HER activity. That is, when scraping off the exterior surface layer (WS_2/GR-S1) with the mass loss of 2.8 mg, the HER activity was only slightly influenced. In contrast, further scraping off the inner part (WS_2/GR-S2) induced a significant degradation of the HER performance, even the mass loss was only 0.74 mg (Fig. 10c, d).

5.3.2 Heterostructures of 1T TMDs and Other Electrocatalysts

Apart from the above strategies, further improved HER performance can be obtained by rationally constructing the heterostructures of 1T TMDs and other electrocatalytic materials, such as metal nanoparticles, transition metal oxides, or carbides (TMOs/TMCs).

With the decoration of Pd, Rh [173], Ni [174], Co [103] nanoparticles, or polymer carbon nanodots [175] on 1T TMDs, the strength of the S/Se-H bonds is weakened with proliferated active sites and accelerated electron transfer. These changes could facilitate the recombination of protons and the release of H_2 and lead to a positive shift of the onset potential and a decrease of Tafel slope. Besides, the nanoparticles present on the TMDs could promote charge transportation from the TMD materials to the electrolyte and enhance the stability of the catalyst in multiple pH conditions [173].

The heterostructures of 1T TMDs and transition metal oxides (or carbides) possess flexible morphology, functionalized surfaces, and unusually chemical/electronic coupling at the interfaces [176–178]. All of these features could contribute to an efficient and durable HER performance. For instance, N-doped $MoSe_2$/TiC-C shell/core arrays with coexisted 1T and 2H $MoSe_2$ were fabricated by Deng et al. [176] via the CVD synthesis of TiC-C arrays on Ti_6Al_4V foils followed by hydrothermal growth and NH_3 treatment of $MoSe_2$ (Fig. 11a). The unique composite material exhibited

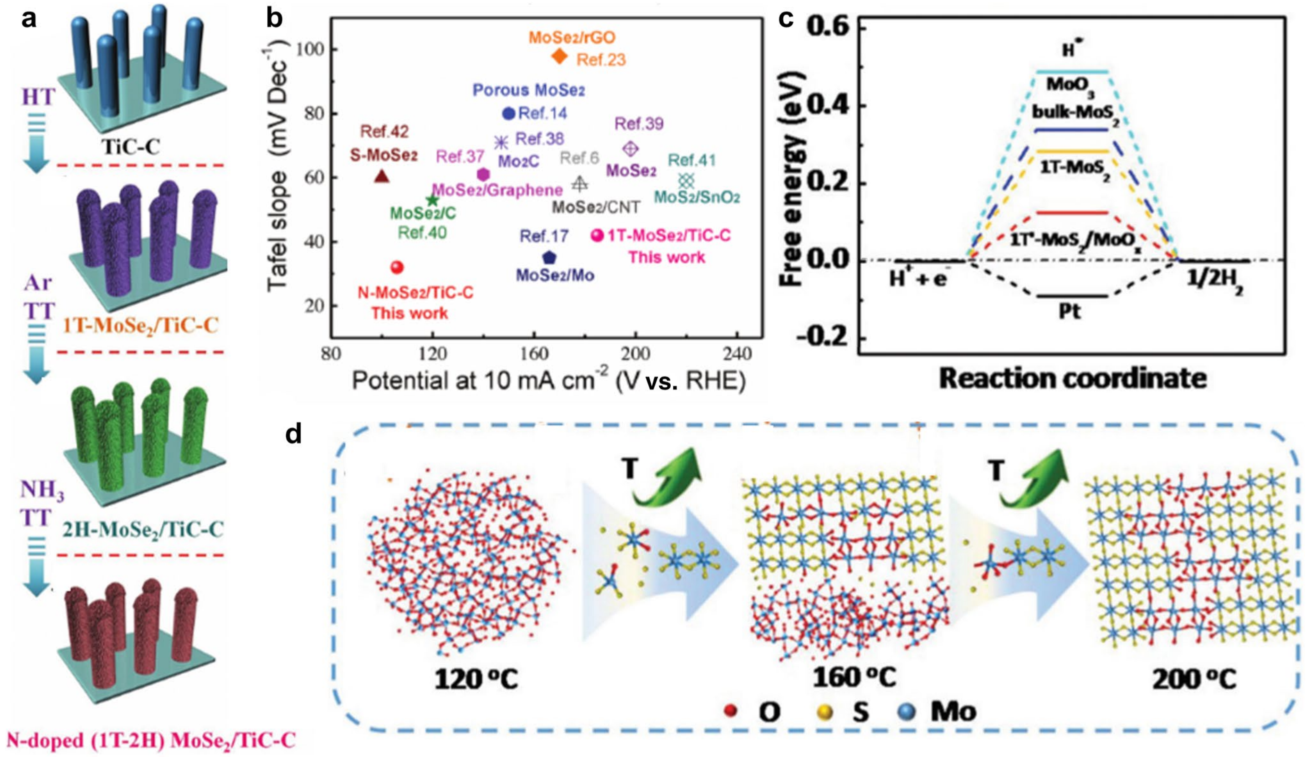

Fig. 11 **a** Schematic illustration of the synthesis of N-$MoSe_2$/TiC-C arrays; **b** HER performance comparison of different Mo-based materials. Reproduced with permission from Ref. [176]. Copyright 2018, John Wiley and Sons. **c** Calculated hydrogen binding energy diagram of the catalyst samples; **d** schematic diagram of the formation process with temperature changes. Reproduced with permission from Ref. [177]. Copyright 2018, The Royal Society of Chemistry

Table 1 HER activities of some representative 1T/1T′ TMD-based materials

Catalysts	Ratio of 1T phase	Electrolytes	Onset potential (mV)	Overpotential (mV) at current density (mA cm^{-2})		Tafel slope (mV dec^{-1})	Exchanged current density (mA cm^{-2})	Turnover frequency (s^{-1})	The number of active sites or C_{dl} (mF cm^{-2})	References
Chemically exfoliated 1T-MoS_2	N/A	0.5 M H_2SO_4		187	10	43				[57]
Stained chemically exfoliated WS_2 NS	~80%	0.5 M H_2SO_4	30–60	250	10	55	0.02	175 (288 mV)	$4{:}5 * 10^{14}$ sites cm^{-2}	[58]
Metallic 1T-WS_2 NS	N/A	0.5 M H_2SO_4	75	142	10	70			48	[64]
Conducting WS_2 NS	80%	0.5 M H_2SO_4		100		40				[58]
VS_2 nanoflowers	N/A	0.5 M H_2SO_4	32	58	10	34				[84]
1T-MoS_2	60%	0.5 M H_2SO_4	130	250	50	49				[115]
1T-MoS_2 QDs	92%–97%	0.5 M H_2SO_4		92	10	44	0.416			[116]
OGNs@MoS_2	2.5%	0.5 M H_2SO_4		118	10	73	0.063	0.2		[117]
1T′-D WS_2	66.4%	0.5 M H_2SO_4		200	10	50.4			18.8	[127]
M-MoS_2	N/A	0.5 M H_2SO_4		210	10	44			10.5	[128]
1T-MoS_2 nanoflowers	> 90%	0.5 M H_2SO_4	171	252	10	45	2.56×10^{-3}	0.0053	1	[129]
Hydrothermal 1T-MoS_2-4-180	55%	0.5 M H_2SO_4		152	10	52			27.8	[130]
1T-MoS_2-MMI	> 92%	0.5 M H_2SO_4	170	220	10	47		1.0 (250 mV)	10.78	[132]
		0.1 M KOH	180	250	10	67		1.0 (290 mV)		
1T-MoS_2/CNFs	58%	0.5 M H_2SO_4		80.5	10	38.2				[122]
O-WS_2-1T	N/A	0.5 M H_2SO_4	88			47	0.022			[138]
N-ReS_2-6/CC	N/A	1 M KOH		90	10	85	0.79		4.2	[139]
N-rich 1T′ MoS_2	N/A	0.5 M H_2SO_4		160	10	36			26.8	[140]
N, P codoped exfoliated WS_2	N/A	0.5 M H_2SO_4	11	59	10	35	1.15	0.791	37.1	[141]
Et_2NPh-MoS_2	81%	0.5 M H_2SO_4		347	10	75				[142]
MoSSe	70%	0.5 M H_2SO_4	49	140	10	40				[125]
$Re_{0.55}Mo_{0.45}S_2$	N/A	0.5 M H_2SO_4	90	169	10	56		3.48 (300 mV)		[146]
Nanoporous $W(Se_xS_{1-x})_2$	N/A	0.5 M H_2SO_4	45	110	10	59	1.26		3.0	[147]
Sub-5 nm 1T′ $ReSe_2$ on CNT	N/A	0.5 M H_2SO_4	23	60	10	37	0.3			[99]
Heterogeneous 1T/2H-MoS_2 nanosheets	72%	0.5 M H_2SO_4	120	220	10	61	0.443		56.2	[148]
1T@2H-MoS_2-8 h/C nanosheets	N/A	0.5 M H_2SO_4	42	64	10	49	0.036		45	[150]
1T@2H $MoSe_2$-4 h	N/A	0.5 M H_2SO_4	20	49	10	41			67	[151]
1T/2H-MoS_2	61.5%	0.5 M H_2SO_4		300	48	46			$15.26 * 10^{-3}$	[152]
1T-MoS_2	> 90%	0.5 M H_2SO_4		330	10	70				[153]
in-plane 1T-2H MoS_2	N/A	1 M KOH		320	20	65		13.14 (250 mV)	2.41	[154]
vh-MoS_2 (1T-2H phase)	N/A	0.5 M H_2SO_4	116	202	10	60				[155]
CoSe/$MoSe_2$	N/A	0.5 M H_2SO_4		192	10	62			24.4	[156]
		1 M KOH		115	10	54				

Table 1 (continued)

Catalysts	Ratio of 1T phase	Electrolytes	Onset potential (mV)	Overpotential (mV) at current density (mA cm^{-2})		Tafel slope (mV dec^{-1})	Exchanged current density (mA cm^{-2})	Turnover frequency (s^{-1})	The number of active sites or C_{dl} (mF cm^{-2})	References
MoS_2@Pt scrolls	28%	0.5 M H_2SO_4		125	10	39	0.014			[157]
(Co, Fe, Ni)$_9S_8$ @1T' MoS_2	N/A	1 M KOH		58	10	37.5			143.1	[180]
MoS_2 NS/MWCNT	N/A	0.5 M H_2SO_4	50	155	10	32				[169]
1T-MoS_2/SWNT	60%	0.5 M H_2SO_4	40	108	10	36				[170]
Co-WSe_2/MWNT	72.1%	0.5 M H_2SO_4 1 M KOH		174 241	10 10	37				[171]
N-$MoSe_2$/VG	N/A	0.5 M H_2SO_4	45	98	10	49			136	[172]
MS200	49.6%	0.5 M H_2SO_4	114	177	10	56.2				[149]
WS_2/GR	75%		231	282	10	47.9				[168]
N-doped $MoSe_2$/TiC-C shell/core arrays	N/A	0.5 M H_2SO_4		106 137	10 100	32			57	[176]
HMHSs	N/A	0.5 M H_2SO_4	55	109	10	42				[177]
1 wt% MnO_2/MoS_2	> 90%	0.5 M H_2SO_4		232	10	66				[178]
1T-MoS_2/CoOOH	N/A	0.5 M H_2SO_4		160	10	42				[179]

a low overpotential of 137 mV at a large current density of 100 mA cm^{-2} and a small Tafel slope of 32 mV dec^{-1}, which exceeded the performance of most previously reported Mo-based catalysts and the commercial Pt/C catalyst (Fig. 11b). Besides, DFT calculation showed that coupling MoO_3 with 1T′-MoS_2 yielded a ΔG_{H*} of ~ 0.126 eV (Fig. 11c) [177]. Ultrathin metallic-phase 1T′-MoS_2/MoO_3 heterostructures (HMHSs) obtained with a temperature-controlled solvothermal method (Fig. 11d) demonstrated an η_{10} of 109 mV, a Tafel slope of 42 mV dec^{-1}, and a robust durability for HER [177]. Analogously, MoS_2 and MnO_2 nanosheets could self-assemble into hetero-2D nanohybrids in a colloidal suspension [178]. The uniformly stacked MnO_2/MoS_2 monolayers with 1 wt% MnO_2 (HMM1) exhibited the best HER performance with its efficient interfacial charge transfer, high porosity, and stability.

The combination of 1T TMDs and an OER catalyst allows the formation of bifunctional catalysts for overall water splitting (both HER and OER). For the heterostructure with ultra-stable 1T-phase MoS_2 embedded into CoOOH (MCSO), the 1T MoS_2 accelerated hydrogen evolution, while CoOOH nanosheets promoted oxygen evolution [179]. The CoOOH functioned not only as an electron donor to induce phase transition of MoS_2 but also as a substrate to stabilize the 1T-MoS_2. As both cathode and anode, the MCSO realized efficient water splitting under a power source of 2 V. Also, hybrid nanotube arrays with 1T′-MoS_2 shells and (Co, Fe, Ni)$_9S_8$ (FeCoNi-HNTA) cores were constructed with ternary Fe, Co, Ni-based layered double hydroxide nanowire arrays (FeCoNi-LDH-NWAs) as the self-sacrificing template [180]. In this hybrid, the monoclinic 1T′ shell ensured efficient HER, while the tri-metallic-ion core facilitated the OER process. Owing to the specific composition and the geometry design, FeCoNi-HNTAs presented both an outstanding HER activity with an η_{10} of 58 mV and a Tafel slope of 37.5 mV dec^{-1} in 0.5 M H_2SO_4, and an excellent OER performance with an η_{10} of 184 mV and a Tafel slope of 49.9 mV dec^{-1} in 1 M KOH. When acted as both the anode and cathode, the FeCoNi-HNTAs achieved efficient water splitting at a cell voltage of 1.429 V for 100 h.

6 Conclusion and Future Perspective

An excellent HER catalyst is expected to exhibit highly efficient and low-overpotential H_2 production with long-term durability. Metallic 1T TMDs have shown great promise for efficient electrocatalytic HER, thanks to their large surface area, high conductivity, and rich active sites at both the edges and the basal planes. The HER performance of 1T-involved TMDs catalysts varies with the element type, phase composition, number of defective sites and strains, morphology, and hydrogen coverage, etc. Over the last decade, a series of methods have been developed for the synthesis and morphology control of 1T TMDs. Meanwhile, important strategies, including cation intercalation, heteroatom doping, alloying, covalent functionalization, and alloying effects, have been adopted for mediating and stabilizing the charges on the 1T/1T′ structure. Also, 1T/2H mixed phases and 1T TMD-based heterostructures have been extensively explored for advanced HER.

Despite the remarkable progress in theoretical understanding and experimental construction of 1T TMD-based electrocatalysts for HER (Table 1), considerable efforts are needed to realize the application of 1T TMD materials for industry-scale HER. First, the Mo and W chalcogenides have been most widely studied. With optimal tuning of the metallic 1T phase, superb HER activities have been achieved. However, the relatively poor stability of these group 6 1T TMDs remains a great concern. To achieve the long-term utilization of these fascinating materials, novel structures with optimized 1T structures and stability have to be explored with continuous endeavors.

Also, based on the representative reported work on 1T TMDs for HER (Table 1), 1T-VS_2 nanoflowers, which were seldom explored, exhibited the most excellent HER performance (with an overpotential of 58 mV at the current density of 10 mV cm^{-2}, and a Tafel slop of 34 mV dec^{-1}) in acidic media (0.5 M H_2SO_4). To fully explore the potential of TMD materials, more attention should be paid on TMDs other than MX_2 (M = Mo, W, X = S, Se) in the future.

Meanwhile, it is vital to develop strategies that could realize the precise control of phases, morphology and defects, etc. for an 1T TMD. Additional templates can be introduced to control the phase and morphology [109]. For defect engineering, currently, focused ion beam, either Ar ions [181] or heavy metal ions (Au) [182], which can create point, line, and face defects at a particular position of the TMDs basal plane with a high resolution, especially combined with STEM technology, should be widely employed [105]. Furthermore, some in situ methods for kinetic study, such as scanning electrochemical cell microscopy (SECCM) [183, 184], can be extended to create in situ defective sites. In this way, not only precise control of defects can be achieved, but also the effect of the defective sites could be locally investigated [185].

Last but not least, while most of the 1T TMDs could show excellent HER in an acidic medium, their performances in alkaline or neutral electrolytes are generally poor or not well explored. Enhancing the electrocatalytic activity of 1T TMDs as well as understanding the reaction mechanisms of 1T TMDs in the various electrolytes is essential for the widespread application of these materials. As discussed in Sect. 2.1, the sluggish kinetics of water dissociation under alkaline conditions results in a significantly inhibited hydrogen production. To solve the issue, strategies that could lower the energy barriers for water dissociation on catalyst surfaces in alkaline media should be attempted. For instance, in recent years, with the incorporation of the first row of transition metals (Ni, Co, and Fe) or the doping of rare metals (Ru), 1T TMDs have showed superb HER performances in the alkaline environment [106–108, 186].

Authors' Contributions Yun Hang Hu, Liang Chang and Zhuxing Sun made contributions to the manuscript preparation.

Funding U.S. National Science Foundation (CMMI-1661699) partially supported this work. The support of Charles and Carroll McArthur is also highly appreciated.

Availability of Data and Materials Not applicable.

Code Availability Not applicable.

Compliance with Ethical Standards

Conflict of interest The authors declare no competing financial interest.

References

1. JO'M, B.: The origin of ideas on a hydrogen economy and its solution to the decay of the environment. Int. J. Hydrogen Energy **27**, 731–740 (2002)
2. Popczun, E.J., McKone, J.R., Read, C.G., et al.: Nanostructured nickel phosphide as an electrocatalyst for the hydrogen evolution reaction. J. Am. Chem. Soc. **135**, 9267–9270 (2013)
3. Wang, X., Xu, C., Jaroniec, M., et al.: Anomalous hydrogen evolution behavior in high-pH environment induced by locally generated hydronium ions. Nat. Commun. **10**, 4876 (2019)
4. Hu, Y.H., Ruckenstein, E.: Catalytic conversion of methane to synthesis gas by partial oxidation and CO_2 reforming. Adv. Catal. **48**, 297–345 (2004)
5. Hu, Y.H.: Solid-solution catalysts for CO_2 reforming of methane. Catal. Today **148**, 206–211 (2009)
6. Han, B., Wei, W., Chang, L., et al.: Efficient visible light photocatalytic CO_2 reforming of CH_4. ACS Catal. **6**, 494–497 (2016)
7. Palo, D.R., Dagle, R.A., Holladay, J.D.: Methanol steam reforming for hydrogen production. Chem. Rev. **107**, 3992–4021 (2007)
8. Sun, Z., Fang, S., Lin, Y., et al.: Photo-assisted methanol steam reforming on solid solution of Cu-Zn-Ti oxide. Chem. Eng. J. **375**, 121909 (2019)
9. Li, Y., Li, H., Li, Y., et al.: Fe-B alloy coupled with Fe clusters as an efficient cocatalyst for photocatalytic hydrogen evolution. Chem. Eng. J. **344**, 506–513 (2018)
10. Fang, S., Hu, Y.H.: Recent progress in photocatalysts for overall water splitting. Int. J. Energy Res. **43**, 1082–1098 (2019)
11. Chen, W., Liu, M., Li, X., et al.: Synthesis of 3D mesoporous g-C_3N_4 for efficient overall water splitting under a Z-scheme photocatalytic system. Appl. Surf. Sci. **512**, 145782 (2020)
12. You, B., Sun, Y.J.: Innovative strategies for electrocatalytic water splitting. Acc. Chem. Res. **51**, 1571–1580 (2018)
13. Anantharaj, S., Ede, S.R., Karthick, K., et al.: Precision and correctness in the evaluation of electrocatalytic water splitting: revisiting activity parameters with a critical assessment. Energy Environ. Sci. **11**, 744–771 (2018)

14. Han, B., Hu, Y.H.: Highly efficient temperature-induced visible light photocatalytic hydrogen production from water. J. Phys. Chem. C **119**, 18927–18934 (2015)
15. Fang, S., Sun, Z., Hu, Y.H.: Insights into the thermo-photo catalytic production of hydrogen from water on a low-cost NiO_x-loaded TiO_2 catalyst. ACS Catal. **9**, 5047–5056 (2019)
16. Fang, S., Liu, Y., Sun, Z., et al.: Photocatalytic hydrogen production over Rh-loaded TiO_2: what is the origin of hydrogen and how to achieve hydrogen production from water? Appl. Catal. B **278**, 119316 (2020)
17. Zhu, J., Hu, L., Zhao, P., et al.: Recent advances in electrocatalytic hydrogen evolution using nanoparticles. Chem. Rev. **120**, 851–918 (2019)
18. Zou, X.X., Zhang, Y.: Noble metal-free hydrogen evolution catalysts for water splitting. Chem. Soc. Rev. **44**, 5148–5180 (2015)
19. Tributsch, H., Bennett, J.: Electrochemistry and photochemistry of MoS_2 layer crystals. I. J. Electroanal. Chem. Interfacial Electrochem. **81**, 97–111 (1977)
20. Han, B., Hu, Y.H.: MoS_2 as a co-catalyst for photocatalytic hydrogen production from water. Energy Sci. Eng. **4**, 285–304 (2016)
21. Lin, L., Lei, W., Zhang, S., et al.: Two-dimensional transition metal dichalcogenides in supercapacitors and secondary batteries. Energy Storage Mater. **19**, 408–423 (2019)
22. Wei, W., Sun, K., Hu, Y.H.: An efficient counter electrode material for dye-sensitized solar cells—flower-structured 1T metallic phase MoS_2. J. Mater. Chem. A **4**, 12398–12401 (2016)
23. Cheng, P., Sun, K., Hu, Y.H.: Memristive behavior and ideal memristor of 1T phase MoS_2 nanosheets. Nano Lett. **16**, 572–576 (2016)
24. Cheng, P., Sun, K., Hu, Y.H.: Mechanically-induced reverse phase transformation of MoS_2 from stable 2H to metastable 1T and its memristive behavior. RSC Adv. **6**, 65691–65697 (2016)
25. Li, Y., Duerloo, K.A.N., Wauson, K., et al.: Structural semiconductor-to-semimetal phase transition in two-dimensional materials induced by electrostatic gating. Nat. Commun. **7**, 10761 (2016)
26. Lin, Y.C., Yeh, C.H., Lin, H.C., et al.: Stable 1T tungsten disulfide monolayer and its junctions: growth and atomic structures. ACS Nano **12**, 12080–12088 (2018)
27. Voiry, D., Goswami, A., Kappera, R., et al.: Covalent functionalization of monolayered transition metal dichalcogenides by phase engineering. Nat. Chem. **7**, 45 (2015)
28. Zhang, F., Zhang, H., Krylyuk, S., et al.: Electric-field induced structural transition in vertical $MoTe_2$-and $Mo_{1-x}W_xTe_2$-based resistive memories. Nat. Mater. **18**, 55–61 (2019)
29. Prabhu, P., Jose, V., Lee, J.M.: Design strategies for development of TMD-based heterostructures in electrochemical energy systems. Matter **2**, 526–553 (2020)
30. Lazar, P., Otyepka, M.: Role of the edge properties in the hydrogen evolution reaction on MoS_2. Chem. Eur. J. **23**, 4863–4869 (2017)
31. Chen, X., Gu, Y., Tao, G., et al.: Origin of hydrogen evolution activity on MS_2 (M = Mo or Nb) monolayers. J. Mater. Chem. A **3**, 18898–18905 (2015)
32. Li, Y., Wang, H., Xie, L., et al.: MoS_2 nanoparticles grown on graphene: an advanced catalyst for the hydrogen evolution reaction. J. Am. Chem. Soc. **133**, 7296–7299 (2011)
33. Kibsgaard, J., Chen, Z., Reinecke, B.N., et al.: Engineering the surface structure of MoS_2 to preferentially expose active edge sites for electrocatalysis. Nat. Mater. **11**, 963–969 (2012)
34. Kosmala, T., Coy Diaz, H., Komsa, H.P., et al.: Metallic twin boundaries boost the hydrogen evolution reaction on the basal plane of molybdenum selenotellurides. Adv. Energy Mater. **8**, 1800031 (2018)
35. Masih Das, P., Thiruraman, J.P., Chou, Y.C., et al.: Centimeter-scale nanoporous 2D membranes and Ion transport: porous MoS_2 monolayers in a few-layer matrix. Nano Lett. **19**, 392–399 (2018)
36. Wang, X., Zhang, Y., Si, H., et al.: Single-atom vacancy defect to trigger high-efficiency hydrogen evolution of MoS_2. J. Am. Chem. Soc. **142**, 4298–4308 (2020)
37. Xie, J., Xie, Y.: Structural engineering of electrocatalysts for the hydrogen evolution reaction: order or disorder? ChemCatChem **7**, 2568–2580 (2015)
38. Shi, S., Sun, Z., Hu, Y.H.: Synthesis, stabilization and applications of 2-dimensional 1T metallic MoS_2. J. Mater. Chem. A **6**, 23932–23977 (2018)
39. Sokolikova, M.S., Mattevi, C.: Direct synthesis of metastable phases of 2D transition metal dichalcogenides. Chem. Soc. Rev. **49**, 3952–3980 (2020)
40. Liu, K.H., Zhong, H.X., Li, S.J., et al.: Advanced catalysts for sustainable hydrogen generation and storage via hydrogen evolution and carbon dioxide/nitrogen reduction reactions. Prog. Mater. Sci. **92**, 64–111 (2018)
41. Hu, C., Zhang, L., Gong, J.: Recent progress made in the mechanism comprehension and design of electrocatalysts for alkaline water splitting. Energy Environ. Sci. **12**, 2620–2645 (2019)
42. Tong, W., Forster, M., Dionigi, F., et al.: Electrolysis of low-grade and saline surface water. Nat. Energy **5**, 367–377 (2020)
43. Yu, P., Wang, F., Shifa, T.A., et al.: Earth abundant materials beyond transition metal dichalcogenides: a focus on electrocatalyzing hydrogen evolution reaction. Nano Energy **58**, 244–276 (2019)
44. Mahmood, N., Yao, Y.D., Zhang, J.W., et al.: Electrocatalysts for hydrogen evolution in alkaline electrolytes: mechanisms, challenges, and prospective solutions. Adv. Sci. **5**, 1700464 (2018)
45. Liu, E., Li, J., Jiao, L., et al.: Unifying the hydrogen evolution and oxidation reactions kinetics in base by identifying the catalytic roles of hydroxyl-water-cation adducts. J. Am. Chem. Soc. **141**, 3232–3239 (2019)
46. Durst, J., Siebel, A., Simon, C., et al.: New insights into the electrochemical hydrogen oxidation and evolution reaction mechanism. Energy Environ. Sci. **7**, 2255–2260 (2014)
47. Nørskov, J.K., Bligaard, T., Logadottir, A., et al.: Trends in the exchange current for hydrogen evolution. J. Electrochem. Soc. **152**, J23 (2005)
48. Eftekhari, A.: Electrocatalysts for hydrogen evolution reaction. Int. J. Hydrogen Energy **42**, 11053–11077 (2017)
49. Wang, J., Xu, F., Jin, H., et al.: Non-noble metal-based carbon composites in hydrogen evolution reaction: fundamentals to applications. Adv. Mater. **29**, 1605838 (2017)
50. Jiao, Y., Zheng, Y., Jaroniec, M., et al.: Design of electrocatalysts for oxygen- and hydrogen-involving energy conversion reactions. Chem. Soc. Rev. **44**, 2060–2086 (2015)
51. Eliaz, N., Gileadi, E.: Physical Electrochemistry: Fundamentals, Techniques, and Applications. Wiley, Hoboken (2019)
52. Finn, S.T., Macdonald, J.E.: Contact and support considerations in the hydrogen evolution reaction activity of petaled MoS_2 electrodes. ACS Appl. Mater. Interfaces **8**, 25185–25192 (2016)
53. Yan, Y., Xia, B., Xu, Z., et al.: Recent development of molybdenum sulfides as advanced electrocatalysts for hydrogen evolution reaction. ACS Catal. **4**, 1693–1705 (2014)
54. Watzele, S., Fichtner, J., Garlyyev, B., et al.: On the dominating mechanism of the hydrogen evolution reaction at polycrystalline Pt electrodes in acidic media. ACS Catal. **8**, 9456–9462 (2018)
55. Jiang, K., Liu, B., Luo, M., et al.: Single platinum atoms embedded in nanoporous cobalt selenide as electrocatalyst for accelerating hydrogen evolution reaction. Nat. Commun. **10**, 1743 (2019)

56. Tsai, C., Chan, K., Nørskov, J.K., et al.: Theoretical insights into the hydrogen evolution activity of layered transition metal dichalcogenides. Surf. Sci. **640**, 133–140 (2015)
57. Lukowski, M.A., Daniel, A.S., Meng, F., et al.: Enhanced hydrogen evolution catalysis from chemically exfoliated metallic MoS_2 nanosheets. J. Am. Chem. Soc. **135**, 10274–10277 (2013)
58. Voiry, D., Yamaguchi, H., Li, J., et al.: Enhanced catalytic activity in strained chemically exfoliated WS_2 nanosheets for hydrogen evolution. Nat. Mater. **12**, 850–855 (2013)
59. Guardia, L., Paredes, J.I., Munuera, J.M., et al.: Chemically exfoliated MoS_2 nanosheets as an efficient catalyst for reduction reactions in the aqueous phase. ACS Appl. Mater. Interfaces. **6**, 21702–21710 (2014)
60. Nicolosi, V., Chhowalla, M., Kanatzidis, M.G., et al.: Liquid exfoliation of layered materials. Science **340**, 1226419 (2013)
61. Chou, S.S., Sai, N., Lu, P., et al.: Understanding catalysis in a multiphasic two-dimensional transition metal dichalcogenide. Nat. Commun. **6**, 8311 (2015)
62. Fan, X.L., Yang, Y., Xiao, P., et al.: Site-specific catalytic activity in exfoliated MoS_2 single-layer polytypes for hydrogen evolution: basal plane and edges. J. Mater. Chem. A **2**, 20545–20551 (2014)
63. Voiry, D., Salehi, M., Silva, R., et al.: Conducting MoS_2 nanosheets as catalysts for hydrogen evolution reaction. Nano Lett. **13**, 6222–6227 (2013)
64. Lukowski, M.A., Daniel, A.S., English, C.R., et al.: Highly active hydrogen evolution catalysis from metallic WS_2 nanosheets. Energy Environ. Sci. **7**, 2608–2613 (2014)
65. Tang, Q., Jiang, D.E.: Mechanism of hydrogen evolution reaction on 1T-MoS_2 from first principles. ACS Catal. **6**, 4953–4961 (2016)
66. Ambrosi, A., Sofer, Z., Pumera, M.: 2H → 1T phase transition and hydrogen evolution activity of MoS_2, $MoSe_2$, WS_2 and WSe_2 strongly depends on the MX_2 composition. Chem. Commun. **51**, 8450–8453 (2015)
67. Yin, Y., Han, J., Zhang, Y., et al.: Contributions of phase, sulfur vacancies, and edges to the hydrogen evolution reaction catalytic activity of porous molybdenum disulfide nanosheets. J. Am. Chem. Soc. **138**, 7965–7972 (2016)
68. Zhou, Y.X., Jia, L.P., Feng, Q.L., et al.: $MoTe_2$ nanodendrites based on Mo doped reduced graphene oxide/polyimide composite film for electrocatalytic hydrogen evolution in neutral solution. Electrochim. Acta **229**, 121–128 (2017)
69. McGlynn, J.C., Cascallana-Matias, I., Fraser, J.P., et al.: Molybdenum ditelluride rendered into an efficient and stable electrocatalyst for the hydrogen evolution reaction by polymorphic control. Energy Technol-Ger **6**, 345–350 (2018)
70. Bhat, K.S., Nagaraja, H.S.: Performance evaluation of molybdenum dichalcogenide (MoX_2; X = S, Se, Te) nanostructures for hydrogen evolution reaction. Int. J. Hydrogen Energy **44**, 17878–17886 (2019)
71. Zhuang, P.Y., Sun, Y.Y., Dong, P., et al.: Revisiting the role of active sites for hydrogen evolution reaction through precise defect adjusting. Adv. Funct. Mater. **29**, 1901290 (2019)
72. Eshete, Y.A., Ling, N., Kim, S., et al.: Vertical heterophase for electrical, electrochemical, and mechanical manipulations of layered $MoTe_2$. Adv. Funct. Mater. **29**, 1904504 (2019)
73. Lu, D.L., Ren, X.H., Ren, L., et al.: Direct vapor deposition growth of 1T' $MoTe_2$ on carbon cloth for electrocatalytic hydrogen evolution. ACS Appl. Energy Mater. **3**, 3212–3219 (2020)
74. He, H.Y., He, Z., Shen, Q.: One-pot synthesis of non-precious metal RGO/1T'-$MoTe_2$: Cu heterohybrids for excellent catalytic hydrogen evolution. Mater. Sci. Eng. B Adv. **260**, 114659 (2020)
75. Mc Manus, J.B., Cunningham, G., et al.: Growth of 1T' $MoTe_2$ by thermally assisted conversion of electrodeposited tellurium films. ACS Appl. Energy Mater. **2**, 521–530 (2019)
76. McGlynn, J.C., Dankwort, T., Kienle, L., et al.: The rapid electrochemical activation of $MoTe_2$ for the hydrogen evolution reaction. Nat. Commun. **10**, 4916 (2019)
77. Li, J., Hong, M.L., Sun, L.J., et al.: Enhanced electrocatalytic hydrogen evolution from large-scale, facile-prepared, highly crystalline WTe_2 nanoribbons with weyl semimetallic phase. ACS Appl. Mater. Interfaces. **10**, 458–467 (2018)
78. Habib, M.R., Wang, S.P., Wang, W.J., et al.: Electronic properties of polymorphic two-dimensional layered chromium disulphide. Nanoscale **11**, 20123–20132 (2019)
79. Kobayashi, S., Katayama, N., Manjo, T., et al.: Linear trimer formation with antiferromagnetic ordering in 1T-$CrSe_2$ originating from peierls-like instabilities and interlayer Se-Se interactions. Inorg. Chem. **58**, 14304–14315 (2019)
80. Lasek, K., Coelho, P.M., Zberecki, K., et al.: Molecular beam epitaxy of transition metal (Ti-, V-, and Cr-) tellurides: from monolayer ditellurides to multilayer self-intercalation compounds. ACS Nano **14**, 8473–8484 (2020)
81. Sun, F., Hong, A., Zhou, W., et al.: Prediction for structure stability and ultrahigh hydrogen evolution performance of monolayer 2H-CrS_2. Mater. Today Commun. **25**, 101707 (2020)
82. Liu, Y., Liang, C., Wu, J., et al.: Atomic layered titanium sulfide quantum dots as electrocatalysts for enhanced hydrogen evolution reaction. Adv. Mater. Interfaces **5**, 1700895 (2018)
83. Hu, P., Long, G., Chaturvedi, A., et al.: Agent-assisted VSSe ternary alloy single crystals as an efficient stable electrocatalyst for the hydrogen evolution reaction. J. Mater. Chem. A **7**, 15714–15721 (2019)
84. Qu, Y., Shao, M., Shao, Y., et al.: Ultra-high electrocatalytic activity of VS_2 nanoflowers for efficient hydrogen evolution reaction. J. Mater. Chem. A **5**, 15080–15086 (2017)
85. Zhang, Y., Chen, X., Huang, Y., et al.: The role of intrinsic defects in electrocatalytic activity of monolayer VS_2 basal planes for the hydrogen evolution reaction. J. Phys. Chem. C **121**, 1530–1536 (2017)
86. Li, H., Tan, Y., Liu, P., et al.: Atomic-sized pores enhanced electrocatalysis of TaS_2 nanosheets for hydrogen evolution. Adv. Mater. **28**, 8945–8949 (2016)
87. Huan, Y., Shi, J., Zou, X., et al.: Scalable production of two-dimensional metallic transition metal dichalcogenide nanosheet powders using NaCl templates toward electrocatalytic applications. J. Am. Chem. Soc. **141**, 18694–18703 (2019)
88. Lai, Z., Chaturvedi, A., Wang, Y., et al.: Preparation of 1T-phase $ReS_{2x}Se_{2(1-x)}$ ($x = 0$-1) nanodots for highly efficient electrocatalytic hydrogen evolution reaction. J. Am. Chem. Soc. **140**, 8563–8568 (2018)
89. Martín-García, B., Spirito, D., Bellani, S., et al.: Extending the colloidal transition metal dichalcogenide library to ReS_2 nanosheets for application in gas sensing and electrocatalysis. Small **15**, 1904670 (2019)
90. Liu, Y., Wu, J., Hackenberg, K.P., et al.: Self-optimizing, highly surface-active layered metal dichalcogenide catalysts for hydrogen evolution. Nat. Energy **2**, 17127 (2017)
91. Pan, H.: Metal dichalcogenides monolayers: novel catalysts for electrochemical hydrogen production. Sci. Rep. **4**, 5348 (2014)
92. Yuan, J., Wu, J., Hardy, W.J., et al.: Facile synthesis of single crystal vanadium disulfide nanosheets by chemical vapor deposition for efficient hydrogen evolution reaction. Adv. Mater. **27**, 5605–5609 (2015)
93. Zhang, H., Liu, L.M., Lau, W.M.: Dimension-dependent phase transition and magnetic properties of VS_2. J. Mater. Chem. A **1**, 10821–10828 (2013)
94. Fan, X., Wang, S., An, Y., et al.: Catalytic activity of MS_2 monolayer for electrochemical hydrogen evolution. J. Phys. Chem. C **120**, 1623–1632 (2016)

95. Shi, J., Wang, X., Zhang, S., et al.: Two-dimensional metallic tantalum disulfide as a hydrogen evolution catalyst. Nat. Commun. **8**, 958 (2017)
96. Hart, L., Dale, S., Hoye, S., et al.: Rhenium dichalcogenides: layered semiconductors with two vertical orientations. Nano Lett. **16**, 1381–1386 (2016)
97. Gao, J., Li, L., Tan, J., et al.: Vertically oriented arrays of ReS_2 nanosheets for electrochemical energy storage and electrocatalysis. Nano Lett. **16**, 3780–3787 (2016)
98. Qi, F., Wang, X., Zheng, B., et al.: Self-assembled chrysanthemum-like microspheres constructed by few-layer $ReSe_2$ nanosheets as a highly efficient and stable electrocatalyst for hydrogen evolution reaction. Electrochim. Acta **224**, 593–599 (2017)
99. Zhuang, M., Xu, G.L., Gan, L.Y., et al.: Sub-5 nm edge-rich $1T'$-$ReSe_2$ as bifunctional materials for hydrogen evolution and sodium-ion storage. Nano Energy **58**, 660–668 (2019)
100. Putungan, D.B., Lin, S.H., Kuo, J.L.: A first-principles examination of conducting monolayer $1T'$-MX_2 ($M=Mo$, W; $X=S$, Se, Te): promising catalysts for hydrogen evolution reaction and its enhancement by strain. Phys. Chem. Chem. Phys. **17**, 21702–21708 (2015)
101. Chen, X., Wang, G.: Tuning the hydrogen evolution activity of MS_2 ($M=Mo$ or Nb) monolayers by strain engineering. Phys. Chem. Chem. Phys. **18**, 9388–9395 (2016)
102. Shang, B., Cui, X.Q., Jiao, L., et al.: Lattice-mismatch-induced ultrastable 1T-phase MoS_2-Pd/Au for plasmon-enhanced hydrogen evolution. Nano Lett. **19**, 2758–2764 (2019)
103. Zheng, X.L., Zhang, G.Y., Xu, X.P., et al.: Synergistic effect of mechanical strain and interfacial-chemical interaction for stable 1T-WSe_2 by carbon nanotube and cobalt. Appl. Surf. Sci. **496**, 143694 (2019)
104. Lu, W.G., Birmingham, B., Zhang, Z.R.: Defect engineering on MoS_2 surface with argon ion bombardments and thermal annealing. Appl. Surf. Sci. **532**, 147461 (2020)
105. Chen, J., Ryu, G.H., Zhang, Q.Y., et al.: Spatially controlled fabrication and mechanisms of atomically thin nanowell patterns in bilayer WS_2 using in situ high temperature electron microscopy. ACS Nano **13**, 14486–14499 (2019)
106. Zhang, J.M., Xu, X.P., Yang, L., et al.: Single-atom Ru doping induced phase transition of MoS_2 and S vacancy for hydrogen evolution reaction. Small Methods **3**, 1900653 (2019)
107. Cao, D.F., Ye, K., Moses, O.A., et al.: Engineering the in-plane structure of metallic phase molybdenum disulfide via Co and O dopants toward efficient alkaline hydrogen evolution. ACS Nano **13**, 11733–11740 (2019)
108. Huang, Y.C., Sun, Y.H., Zheng, X.L., et al.: Atomically engineering activation sites onto metallic 1T-MoS_2 catalysts for enhanced electrochemical hydrogen evolution. Nat. Commun. **10**, 982 (2019)
109. He, Y.M., Tang, P.Y., Hu, Z.L., et al.: Engineering grain boundaries at the 2D limit for the hydrogen evolution reaction. Nat. Commun. **11**, 57 (2020)
110. Zhao, X., Ma, X., Sun, J., et al.: Enhanced catalytic activities of surfactant-assisted exfoliated WS2 nanodots for hydrogen evolution. ACS Nano **10**, 2159–2166 (2016)
111. Qu, Y., Pan, H., Kwok, C.T.: Hydrogenation-controlled phase transition on two-dimensional transition metal dichalcogenides and their unique physical and catalytic properties. Sci. Rep. **6**, 34186 (2016)
112. Luxa, J., Vosecký, P., Mazánek, V., et al.: Cation-controlled electrocatalytical activity of transition-metal disulfides. ACS Catal. **8**, 2774–2781 (2018)
113. Chia, X., Ambrosi, A., Sedmidubský, D., et al.: Precise tuning of the charge transfer kinetics and catalytic properties of MoS_2 materials via electrochemical methods. Chem. Eur. J. **20**, 17426–17432 (2014)
114. Leong, S.X., Mayorga-Martinez, C.C., Chia, X., et al.: 2H → 1T phase change in direct synthesis of WS2 nanosheets via solution-based electrochemical exfoliation and their catalytic properties. ACS Appl. Mater. Interfaces **9**, 26350–26356 (2017)
115. Ejigu, A., Kinloch, I.A., Prestat, E., et al.: A simple electrochemical route to metallic phase trilayer MoS_2: evaluation as electrocatalysts and supercapacitors. J. Mater. Chem. A **5**, 11316–11330 (2017)
116. Chen, W., Gu, J., Liu, Q., et al.: Quantum dots of 1T phase transitional metal dichalcogenides generated via electrochemical Li intercalation. ACS Nano **12**, 308–316 (2018)
117. Nguyen, V.T., Le, P.A., Hsu, Y.C., et al.: Plasma-induced exfoliation provides onion-like graphene-surrounded MoS_2 nanosheets for a highly efficient hydrogen evolution reaction. ACS Appl. Mater. Interfaces. **12**, 11533–11542 (2020)
118. Tang, Q.: Tuning the phase stability of Mo-based TMD monolayers through coupled vacancy defects and lattice strain. J. Mater. Chem. C **6**, 9561–9568 (2018)
119. Patra, T.K., Zhang, F., Schulman, D.S., et al.: Defect dynamics in 2-D MoS_2 probed by using machine learning, atomistic simulations, and high-resolution microscopy. ACS Nano **12**, 8006–8016 (2018)
120. Zhu, J.Q., Wang, Z.C., Yu, H., et al.: Argon plasma induced phase transition in monolayer MoS_2. J. Am. Chem. Soc. **139**, 10216–10219 (2017)
121. Gan, X.R., Lee, L.Y.S., Wong, K.Y., et al.: 2H/1T phase transition of multilayer MoS_2 by electrochemical incorporation of S vacancies. ACS Appl. Energy Mater. **1**, 4754–4765 (2018)
122. Nam, D.H., Kim, J.Y., Kang, S., et al.: Anion extraction-induced polymorph control of transition metal dichalcogenides. Nano Lett. **19**, 8644–8652 (2019)
123. Radisavljevic, B., Radenovic, A., Brivio, J., et al.: Single-layer MoS_2 transistors. Nat. Nanotechnol. **6**, 147–150 (2011)
124. Coleman, J.N., Lotya, M., O'Neill, A., et al.: Two-dimensional nanosheets produced by liquid exfoliation of layered materials. Science **331**, 568–571 (2011)
125. Tan, C.L., Luo, Z.M., Chaturvedi, A., et al.: Preparation of high-percentage 1T-phase transition metal dichalcogenide nanodots for electrochemical hydrogen evolution. Adv. Mater. **30**, 1705509 (2018)
126. Chua, C.K., Loo, A.H., Pumera, M.: Top-down and bottom-up approaches in engineering 1T phase molybdenum disulfide (MoS_2): towards highly catalytically active materials. Chem. Eur. J. **22**, 14336–14341 (2016)
127. Liu, Z., Li, N., Su, C., et al.: Colloidal synthesis of 1T' phase dominated WS_2 towards endurable electrocatalysis. Nano Energy **50**, 176–181 (2018)
128. Wang, J., Wang, N., Guo, Y., et al.: Metallic-phase MoS_2 nanopetals with enhanced electrocatalytic activity for hydrogen evolution. ACS Sustain. Chem. Eng. **6**, 13435–13442 (2018)
129. Venkateshwaran, S., Senthil Kumar, S.M.: Template-driven phase selective formation of metallic 1T-MoS_2 nanoflowers for hydrogen evolution reaction. ACS Sustain. Chem. Eng. **7**, 2008–2017 (2018)
130. Yin, Y., Zhang, Y., Gao, T., et al.: Synergistic phase and disorder engineering in 1T-$MoSe_2$ nanosheets for enhanced hydrogen evolution reaction. Adv. Mater. **29**, 1700311 (2017)
131. Gao, G., Jiao, Y., Ma, F., et al.: Charge mediated semiconducting-to-metallic phase transition in molybdenum disulfide monolayer and hydrogen evolution reaction in new 1T' phase. J. Phys. Chem. C **119**, 13124–13128 (2015)
132. Park, S., Kim, C., Park, S.O., et al.: Phase engineering of transition metal dichalcogenides with unprecedentedly high phase

purity, stability, and scalability via molten-metal-assisted intercalation. Adv. Mater. **32**, 2001889 (2020)

133. Attanayake, N.H., Thenuwara, A.C., Patra, A., et al.: Effect of intercalated metals on the electrocatalytic activity of 1T-MoS_2 for the hydrogen evolution reaction. ACS Energy Lett. **3**, 7–13 (2018)
134. Liu, S., Li, M., Wang, C., et al.: Tuning the electronic structure of Se via constructing Rh-$MoSe_2$ nanocomposite to generate high-performance electrocatalysis for hydrogen evolution reaction. ACS Sustain. Chem. Eng. **6**, 9137–9144 (2018)
135. Chia, X., Sutrisnoh, N.A.A., Sofer, Z., et al.: Morphological effects and stabilization of the metallic 1T phase in layered V-, Nb-, and Ta-doped WSe_2 for electrocatalysis. Chem. Eur. J. **24**, 3199–3208 (2018)
136. Huang, C., Wang, X., Wang, D., et al.: Atomic pillar effect in Pd_xNbS_2 to boost basal plane activity for stable hydrogen evolution. Chem. Mater. **31**, 4726–4731 (2019)
137. Ji, L., Yan, P., Zhu, C., et al.: One-pot synthesis of porous 1T-phase MoS_2 integrated with single-atom Cu doping for enhancing electrocatalytic hydrogen evolution reaction. Appl. Catal. B **251**, 87–93 (2019)
138. Sarma, P.V., Tiwary, C.S., Radhakrishnan, S., et al.: Oxygen incorporated WS_2 nanoclusters with superior electrocatalytic properties for hydrogen evolution reaction. Nanoscale **10**, 9516–9524 (2018)
139. Sun, Q., Zhang, B., Diao, L., et al.: Engineering the electronic structure of 1T'-ReS_2 through nitrogen implantation for enhanced alkaline hydrogen evolution. J. Mater. Chem. A **8**, 11607–11616 (2020)
140. Kwak, I.H., Kwon, I.S., Abbas, H.G., et al.: Nitrogen-rich 1T′-MoS_2 layered nanostructures using alkyl amines for high catalytic performance toward hydrogen evolution. Nanoscale **10**, 14726–14735 (2018)
141. Maiti, A., Srivastava, S.K.: Sulphur edge and vacancy assisted nitrogen–phosphorus co-doped exfoliated tungsten disulfide: a superior electrocatalyst for hydrogen evolution reaction. J. Mater. Chem. A **6**, 19712–19726 (2018)
142. Benson, E.E., Zhang, H., Schuman, S.A., et al.: Balancing the hydrogen evolution reaction, surface energetics, and stability of metallic MoS_2 nanosheets via covalent functionalization. J. Am. Chem. Soc. **140**, 441–450 (2018)
143. Linghu, Y., Li, N., Du, Y., et al.: Ligand induced structure and property changes of 1T-MoS_2. Phys. Chem. Chem. Phys. **21**, 9391–9398 (2019)
144. Pandey, M., Jacobsen, K.W., Thygesen, K.S.: Atomically thin ordered alloys of transition metal dichalcogenides: stability and band structures. J. Phys. Chem. C **120**, 23024–23029 (2016)
145. Chen, Y., Zhang, J., Guo, P., et al.: Coupled heterostructure of Mo-Fe selenide nanosheets supported on carbon paper as an integrated electrocatalyst for efficient hydrogen evolution. ACS Appl. Mater. Interfaces. **10**, 27787–27794 (2018)
146. Yang, S.Z., Gong, Y., Manchanda, P., et al.: Rhenium-doped and stabilized MoS_2 atomic layers with basal-plane catalytic activity. Adv. Mater. **30**, 1803477 (2018)
147. Liang, K., Yan, Y., Guo, L., et al.: Strained $W(Se_xS_{1-x})_2$ nanoporous films for highly efficient hydrogen evolution. ACS Energy Lett. **2**, 1315–1320 (2017)
148. Liu, Z., Gao, Z., Liu, Y., et al.: Heterogeneous nanostructure based on 1T-phase MoS_2 for enhanced electrocatalytic hydrogen evolution. ACS Appl. Mater. Interfaces. **9**, 25291–25297 (2017)
149. Sun, Z., Yang, M., Wang, Y., et al.: Novel binder-free three-dimensional MoS_2-based electrode for efficient and stable electrocatalytic hydrogen evolution. ACS Appl. Energy Mater. **2**, 1102–1110 (2019)
150. Shi, S., Gao, D., Xia, B., et al.: Enhanced hydrogen evolution catalysis in MoS_2 nanosheets by incorporation of a metal phase. J. Mater. Chem. A **3**, 24414–24421 (2015)
151. Zhang, J., Wang, T., Liu, P., et al.: Enhanced catalytic activities of metal-phase-assisted 1T@2H-$MoSe_2$ nanosheets for hydrogen evolution. Electrochim. Acta **217**, 181–186 (2016)
152. Wang, D., Zhang, X., Bao, S., et al.: Phase engineering of a multiphasic 1T/2H MoS_2 catalyst for highly efficient hydrogen evolution. J. Mater. Chem. A **5**, 2681–2688 (2017)
153. Tong, X., Qi, Y., Chen, J., et al.: Supercritical CO_2-assisted reverse-micelle-induced solution-phase fabrication of two-dimensional metallic 1T-MoS_2 and 1T-WS_2. ChemNanoMat **3**, 466–471 (2017)
154. Wang, S., Zhang, D., Li, B., et al.: Ultrastable in-plane 1T–2H MoS_2 heterostructures for enhanced hydrogen evolution reaction. Adv. Energy Mater. **8**, 1801345 (2018)
155. Yang, J., Wang, K., Zhu, J., et al.: Self-templated growth of vertically aligned 2H-1T MoS_2 for efficient electrocatalytic hydrogen evolution. ACS Appl. Mater. Interfaces. **8**, 31702–31708 (2016)
156. Song, W., Wang, K., Jin, G., et al.: Two-step hydrothermal synthesis of CoSe/$MoSe_2$ as hydrogen evolution electrocatalysts in acid and alkaline electrolytes. Chem ElectroChem. **6**, 4842–4847 (2019)
157. Choi, K.H., Park, J.E., Suh, D.H.: Highly efficient hydrogen evolution reaction by strain and phase engineering in composites of Pt and MoS_2 nano-scrolls. Phys. Chem. Chem. Phys. **19**, 18356–18365 (2017)
158. He, Q., Wang, L., Yin, K., et al.: Vertically aligned ultrathin 1T-WS_2 nanosheets enhanced the electrocatalytic hydrogen evolution. Nanoscale Res. Lett. **13**, 167 (2018)
159. Voiry, D., Fullon, R., Yang, J., et al.: The role of electronic coupling between substrate and 2D MoS_2 nanosheets in electrocatalytic production of hydrogen. Nat. Mater. **15**, 1003–1009 (2016)
160. Yu, Q., Luo, Y., Qiu, S., et al.: Tuning the hydrogen evolution performance of metallic 2D tantalum disulfide by interfacial engineering. ACS Nano **13**, 11874–11881 (2019)
161. Lee, Y.B., Kim, S.K., Ji, S., et al.: Facile microwave assisted synthesis of vastly edge exposed 1T/2H-MoS_2 with enhanced activity for hydrogen evolution catalysis. J. Mater. Chem. A **7**, 3563–3569 (2019)
162. Wang, H., Lu, Z., Kong, D., et al.: Electrochemical tuning of MoS_2 nanoparticles on three-dimensional substrate for efficient hydrogen evolution. ACS Nano **8**, 4940–4947 (2014)
163. Xiang, Z., Zhang, Z., Xu, X., et al.: MoS_2 nanosheets array on carbon cloth as a 3D electrode for highly efficient electrochemical hydrogen evolution. Carbon **98**, 84–89 (2016)
164. Qiao, J., Song, F., Hu, J., et al.: Ultrathin MoSSe alloy nanosheets anchored on carbon nanotubes as advanced catalysts for hydrogen evolution. Int. J. Hydrogen Energy **44**, 16110–16119 (2019)
165. Liu, Y., Liu, J., Li, Z., et al.: Exfoliated MoS_2 with porous graphene nanosheets for enhanced electrochemical hydrogen evolution. Int. J. Hydrogen Energy **43**, 13946–13952 (2018)
166. Hui, L., Xue, Y., He, F., et al.: Efficient hydrogen generation on graphdiyne-based heterostructure. Nano Energy **55**, 135–142 (2019)
167. Xiong, J., Li, J., Shi, J., et al.: Metallic 1T-MoS_2 nanosheets in situ entrenched on N, P, S-codoped hierarchical carbon microflower as an efficient and robust electro-catalyst for hydrogen evolution. Appl. Catal. B **243**, 614–620 (2019)
168. Yang, M., Sun, Z., Hu, Y.H.: Novel WS_2-based 3D electrode with protecting scaffold for efficient and stable hydrogen evolution. J. Phys. Chem. C **123**, 12142–12148 (2019)
169. Cao, J., Zhou, J., Zhang, Y., et al.: A clean and facile synthesis strategy of MoS_2 nanosheets grown on multi-wall CNTs for

enhanced hydrogen evolution reaction performance. Sci. Rep. **7**, 8825 (2017)

170. Liu, Q., Fang, Q., Chu, W., et al.: Electron-doped 1T-MoS_2 via interface engineering for enhanced electrocatalytic hydrogen evolution. Chem. Mater. **29**, 4738–4744 (2017)
171. Zhang, G., Zheng, X., Xu, Q., et al.: Carbon nanotube-induced phase and stability engineering: a strained cobalt-doped WSe_2/MWNT heterostructure for enhanced hydrogen evolution reaction. J. Mater. Chem. A **6**, 4793–4800 (2018)
172. Deng, S., Zhong, Y., Zeng, Y., et al.: Directional construction of vertical nitrogen-doped 1T–2H $MoSe_2$/graphene shell/core nanoflake arrays for efficient hydrogen evolution reaction. Adv. Mater. **29**, 1700748 (2017)
173. Sharma, M.D., Mahala, C., Basu, M.: Nanosheets of $MoSe_2$@M (M = Pd and Rh) function as widespread pH tolerable hydrogen evolution catalyst. J. Colloid Interf. Sci. **534**, 131–141 (2019)
174. Hao, Y., Wang, Y.T., Xu, L.C., et al.: 1T-MoS_2 monolayer doped with isolated Ni atoms as highly active hydrogen evolution catalysts: a density functional study. Appl. Surf. Sci. **469**, 292–297 (2019)
175. Kagkoura, A., Canton-Vitoria, R., Vallan, L., et al.: Bottom-up synthesized MoS_2 interfacing polymer carbon nanodots with electrocatalytic activity for hydrogen evolution. Chem. Eur. J. **26**, 6635–6642 (2020)
176. Deng, S., Yang, F., Zhang, Q., et al.: Phase modulation of (1T–2H)-$MoSe_2$/TiC-C shell/core arrays via nitrogen doping for highly efficient hydrogen evolution reaction. Adv. Mater. **30**, 1802223 (2018)
177. Xue, X., Zhang, J., Saana, I.A., et al.: Rational inert-basal-plane activating design of ultrathin 1T′ phase MoS_2 with a MoO_3 heterostructure for enhancing hydrogen evolution performances. Nanoscale **10**, 16531–16538 (2018)
178. Jin, X., Shin, S.-J., Kim, J., et al.: Heterolayered 2D nanohybrids of uniformly stacked transition metal dichalcogenide-transition metal oxide monolayers with improved energy-related functionalities. J. Mater. Chem. A **6**, 15237–15244 (2018)
179. Shang, B., Ma, P., Fan, J., et al.: Stabilized monolayer 1T MoS_2 embedded in CoOOH for highly efficient overall water splitting. Nanoscale **10**, 12330–12336 (2018)
180. Li, H., Chen, S., Zhang, Y., et al.: Systematic design of superaerophobic nanotube-array electrode comprised of transition-metal sulfides for overall water splitting. Nat. Commun. **9**, 2452 (2018)
181. Huang, W.T., Zhou, Q.W., Su, S.Q., et al.: Ion beam defect engineering on ReS_2/Si photocathode with significantly enhanced hydrogen evolution reaction. Adv. Mater. Interfaces **6**, 1801663 (2019)
182. He, Z.Y., Zhao, R., Chen, X.F., et al.: Defect engineering in single-layer MoS_2 using heavy ion irradiation. ACS Appl. Mater. Interfaces. **10**, 42524–42533 (2018)
183. Bentley, C.L., Kang, M., Maddar, F.M., et al.: Electrochemical maps and movies of the hydrogen evolution reaction on natural crystals of molybdenite (MoS_2): basal vs. edge plane activity. Chem. Sci. **8**, 6583–6593 (2017)
184. Takahashi, Y., Kobayashi, Y., Wang, Z.Q., et al.: High-resolution electrochemical mapping of the hydrogen evolution reaction on transition-metal dichalcogenide nanosheets. Angew. Chem. Int. Ed. **59**, 3601–3608 (2020)
185. Hill, J.W., Fu, Z.G., Tian, J.F., et al.: Locally engineering and interrogating the photoelectrochemical behavior of defects in transition metal dichalcogenides. J. Phys. Chem. C **124**, 17141–17149 (2020)
186. Zhang, X., Zhang, Y.Y., Zhang, Y., et al.: Phase-controlled synthesis of 1T-$MoSe_2$/NiSe heterostructure nanowire arrays via electronic injection for synergistically enhanced hydrogen evolution. Small Methods **3**, 1800317 (2019)

Liang Chang received her bachelor's and master's degrees from Wuhan University of Technology in 2010 and 2012, respectively. She became a Ph.D. graduate student in Prof. Yun Hang Hu's group at Michigan Technological University (USA) in 2013 and obtained a Ph.D. degree in 2018. Then, as a postdoctoral fellow, she joined Prof. Allen Bard's group at the University of Texas at Austin. Her research focuses on advanced materials for electrochemical applications, such as supercapacitors, capacitive deionization, batteries, and electrocatalysis.

Zhuxing Sun is a postdoctoral researcher working for Prof. Yun Hang Hu at Michigan Technological University (USA). She received her PhD degree at Zhejiang University (China) in 2017 and was a visiting scholar in Prof. Lianzhou Wang's group at the University of Queensland (Australia) from 2015 to 2016. Her research interest focuses on the synthesis of advanced 2D materials for energy conversion and contaminant remediation.

Yun Hang Hu is the Charles and Carroll McArthur Endowed Chair Professor at Michigan Technological University. He is a fellow of the American Association for the Advancement of Science (AAAS), a fellow of the American Chemical Society (ACS), a fellow of the American Physical Society (APS), a fellow of the American Institute of Chemical Engineers (AIChE), a fellow of the ASM International (ASM), and a fellow of the Royal Society of Chemistry (RSC). He was elected as the chair of the Energy and Fuels Division of ACS in 2014 and the president of the Hydrogen Storage Division of the International Association for Hydrogen Energy (IAHE) in 2015. He is the editor-in-chief of "*Energy Science & Engineering*" (Wiley journal) and an editorial board member for 8 international journals. His main research interests range from nanomaterials, clean fuels, solar energy, batteries, supercapacitors, and hydrogen storage materials to CO_2 conversion.